

Formation and Dissociation of Field-Linked Tetramers

Fulin Deng,^{1,2} Xing-Yan Chen,^{3,4} Xin-Yu Luo,^{3,4} Wenxian Zhang,^{1,5} Su Yi,^{2,6,7,*} and Tao Shi^{2,6,†}

¹*School of Physics and Technology, Wuhan University, Wuhan, Hubei 430072, China*

²*CAS Key Laboratory of Theoretical Physics, Institute of Theoretical Physics, Chinese Academy of Sciences, Beijing 100190, China*

³*Max-Planck-Institut für Quantenoptik, 85748 Garching, Germany*

⁴*Munich Center for Quantum Science and Technology, 80799 München, Germany*

⁵*Wuhan Institute of Quantum Technology, Wuhan, Hubei 430206, China*

⁶*CAS Center for Excellence in Topological Quantum Computation & School of Physical Sciences, University of Chinese Academy of Sciences, Beijing 100049, China*

⁷*Peng Huanwu Collaborative Center for Research and Education, Beihang University, Beijing 100191, China*
(Dated: May 24, 2024)

We investigate the static and dynamic properties of tetratomic molecules formed by two microwave-shielded polar molecules across field-linked resonances. In particular, we focus on two-body physics and experimental techniques unexplored in the recent experiment [X.-Y. Chen *et al.*, Nature **626**, 283 (2024)]. We show that, compared to the lowest tetramer state, higher tetramer states typically have longer lifetimes, which may facilitate a further cooling of tetramer gases towards quantum degeneracy. To detect tetramers, we identify the distinctive time-of-flight images from ramp dissociation, which can be observed by lowering the ramp rate of the microwave. Remarkably, in the modulational dissociation of tetramers, we find that multi-photon processes induce dissociation even below the threshold modulation frequency when the modulation amplitude is sufficiently high. Given the universal form of the inter-molecular potential for microwave-shielded polar molecules, our results also apply to other molecular gases widely explored in recent experiments.

Introduction.—Ultracold molecules [1, 2], with their abundant internal and external degrees of freedom, offer an exceptional avenue for exploring quantum dynamics [3, 4], controlling chemical reactions [5–7], and enabling a wide range of applications in quantum computing [8, 9], quantum simulation [10, 11], quantum information processing [12–15], and precision measurement [16–19]. After over a decade of extensive efforts [20–34], ultracold Bose and degenerate Fermi gases of molecules have been successfully achieved in experiments [35–42] through microwave shielding techniques. The stable molecular gases provide an ideal platform for investigating novel scattering processes [43–46] and intriguing many-body effects [47–57] induced by long-range anisotropic dipole-dipole interactions (DDI).

Remarkably, both DDI and the short-range shielding potential between microwave-shielded molecules (MSMs) can be effectively manipulated by the elliptic angle and Rabi frequency of the microwave field, leading to field-linked (FL) scattering resonances [38, 57]. The adiabatical ramping of microwave field across FL resonances, a tetratomic molecule composed of two MSMs can be formed. Although the tetramer has been proposed theoretically for bosonic molecules [58], the first stable ultracold FL tetramer (NaK)₂ is realized experimentally [46] in a fermionic NaK gas, benefiting from Pauli-blocking and reduced collisional losses [59] via microwave-shielding. The fermionic MSMs emerge as promising candidates for investigating unprecedented strongly correlated physics in the crossover from *p*-wave Bardeen-Cooper-Schrieffer (BCS) superfluidities of molecules to Bose-Einstein condensations (BEC) of

tetramers [55, 56, 60, 61].

In this Letter, we investigate the static and dynamic properties of the FL tetramer formed by two fermionic MSMs, focusing on properties and experimental techniques unexplored in the recent experiment [46]. We study the binding energy and lifetime of p_x tetramers which differ in spatial symmetry from the p_y tetramers realized in [46]. Remarkably, the longer lifetimes of p_x tetramers (e.g., 10.4s for LiRb molecules) show promise for cooling tetramers to quantum degeneracy. By studying tetramer dissociation, we find that the featured time-of-flight images of tetramer wavefunctions can be observed in ramp dissociation (RD) by lowering the microwave ramping rate. In modulational dissociation (MD), large modulations of the elliptic angle lead to tetramer dissociation below the threshold modulation frequency, linked to multiple-photon processes.

Models for two MSMs.—As a concrete example, we consider the NaK molecules which are treated as rigid rotors with electric dipole moment d . At ultracold temperature, only the lowest four rotational manifolds that consist of four rotational states are of relevance. To achieve microwave shielding, molecules are illuminated by a microwave field blue detuned from the transition frequency of the lowest and the first excited rotational levels. The interaction potential between molecules in the highest dressed state, $|+\rangle$, is then consistently repulsive at short distance, preventing molecules from forming an unstable complex.

For the model of two molecules, we first note that the

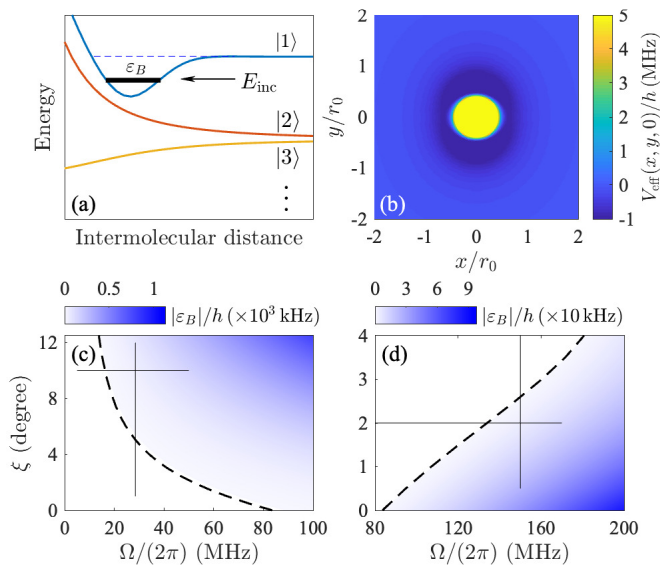


FIG. 1. (a) Schematic of the adiabatic curves of two interacting molecules. The bold black line denotes a bound state and the arrow marks the incident energy. (b) A typical effective potential on the x - y plane with $\Omega/(2\pi) = 130$ MHz and $\xi = 2^\circ$. (c) and (d) are distributions of the binding energies for, respectively, the p_y - and p_x -tetramer states on the Ω - ξ plane. The dashed lines in (c) and (d) denote the positions of shape resonances. The vertical and horizontal lines denote the ranges of the control parameters being ramped in tetramer association and dissociation.

inter-molecular DDI is

$$V(\mathbf{r}) = \frac{d^2}{4\pi\epsilon_0 r^3} \left[\hat{\mathbf{d}}_1 \cdot \hat{\mathbf{d}}_2 - 3(\hat{\mathbf{d}}_1 \cdot \hat{\mathbf{r}})(\hat{\mathbf{d}}_2 \cdot \hat{\mathbf{r}}) \right], \quad (1)$$

where ϵ_0 is the electric permittivity of vacuum, $r = |\mathbf{r}|$, $\hat{\mathbf{r}} = \mathbf{r}/r$, and $\hat{\mathbf{d}}_{j=1,2}$ is the unit vector along the internuclear axis of the j th molecule. Then in the two-molecule Hilbert space with basis states formed by symmetrized dressed states, the $|+\rangle$ state only couples to six lower two-molecule states through DDI [57, 62]. For brevity, we label these seven basis states as $|\nu\rangle$ with $\nu = 1$ to 7 in descending order of energies ($E_\nu^{(\infty)}$) of the asymptotic states. In Fig. 1(a), we schematically show the adiabatic potentials obtained by diagonalizing the interaction matrix in the 7-dimensional Hilbert space.

Although the complete description of two interacting $|+\rangle$ molecules involves all seven channels, the situation is greatly simplified at ultracold temperatures for which the typical timescale for the rotation is much smaller than that of the center-of-mass motion. Consequently, we may focus on the highest potential curve which is the effective potential between MSMs. As shown by us in Ref. [57],

the effective potential can be approximated as

$$V_{\text{eff}}(\mathbf{r}) = \frac{C_6}{r^6} \sin^2 \theta \{ 1 - \mathcal{F}_\xi(\varphi) + [1 - \mathcal{F}_\xi(\varphi)]^2 \cos^2 \theta \} + \frac{C_3}{r^3} [3 \cos^2 \theta - 1 + 3\mathcal{F}_\xi(\varphi) \sin^2 \theta], \quad (2)$$

where $\mathcal{F}_\xi(\varphi) = \sin 2\xi \cos 2\varphi$ with ξ being the ellipticity of the microwave, θ (φ) is the polar (azimuthal) angle of \mathbf{r} , and $C_3 = d^2\Omega^2 / [48\pi\epsilon_0(\Omega^2 + \delta^2)]$ with Ω being the Rabi frequency and δ the detuning of the microwave [62]. As to C_6 , although it is convenient to use the approximate expression $C_6 \approx 18(\Omega^2 + \delta^2)^{1/2}C_3^2$ to analyze the properties of V_{eff} , we adopt, in all numerical calculations, a more accurate C_6 by fitting the adiabatic potential [57]. It should also be noted that Eq. (2) is valid only when $|\xi| \lesssim 15^\circ$ and $r^3 > d^2/(4\pi\epsilon_0\Omega)$.

Among the control parameters of V_{eff} , we shall, for simplicity, fix the detuning at $\delta = -2\pi \times 9.5$ MHz throughout this work, which reduces the control parameters to ξ and Ω . Without loss of generality, we always assume that $\xi \geq 0$. For $\xi = 0$, $V_{\text{eff}}(\mathbf{r})$ is axially symmetric with a circular attractive potential well on the horizontal planes in the vicinity of $z = 0$. However, as shown in Fig. 1(b), this axial symmetry is broken for a nonzero ξ such that the depth of the attractive potential well is increased (lowered) along the y (x) direction. Moreover, for a given ξ , the depth of the potential well grows as Ω is increased. These tunabilities, as demonstrated in Refs. [46, 57], can be used to induce scattering resonances and form bound states.

Now the relative motion of two MSMs is described by the Hamiltonian

$$H_{\text{eff}} = -\frac{\hbar^2 \nabla^2}{M} + V_{\text{eff}}(\mathbf{r}), \quad (3)$$

where M is the mass of the molecule. The validity of this single-channel model was justified by studying scatterings of two $|+\rangle$ molecules [57].

Properties of the tetramer states.—The wavefunction ψ_B of a tetramer states can be obtained by numerically solving the Schrödinger equation

$$H_{\text{eff}}\psi_B = \varepsilon_B\psi_B, \quad (4)$$

where ε_B (< 0) is the binding energy. For $\xi = 0$, the z component of the angular momentum is conserved such that the eigenstates of H_{eff} have a definite quantum number m for the projection of the angular momentum. It is numerically found that bound states emerge when Ω is larger than the critical value $\Omega_c \equiv 2\pi \times 83$ MHz. These bound states are doubly degenerate with respect to $m = \pm 1$ and the bound-state wave functions are $\psi_B^{(\pm)}(\mathbf{r}) = \sum_{\text{odd } l} Y_{l,\pm 1}(\hat{r})\phi_l(r)$, where the radial wave functions ϕ_l are determined numerically. For $\xi > 0$, the degeneracy is lifted and leads to a p_y -tetramer state $\psi_B^{(y)} \propto (\psi_B^{(+)} + \psi_B^{(-)})$ and a p_x -tetramer state $\psi_B^{(x)} \propto$

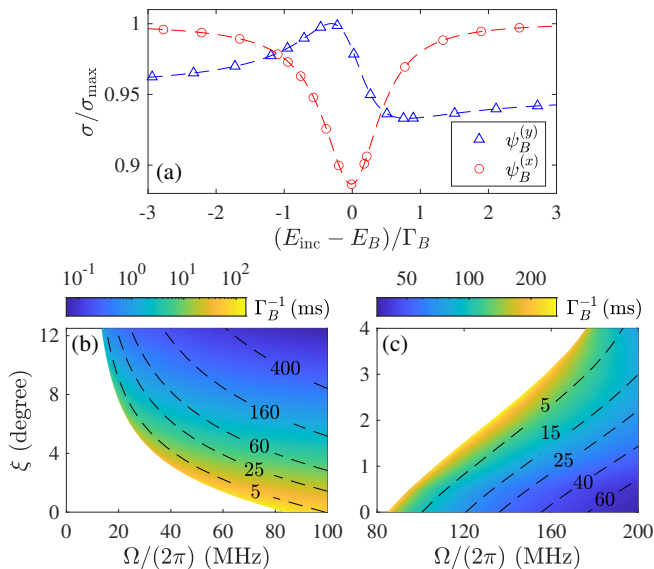


FIG. 2. (a) Scattering cross sections across the resonances associated with $\psi_B^{(y)}$ (\triangle) and $\psi_B^{(x)}$ (\circ) with parameters $(\Omega/(2\pi), \xi) = (19.52 \text{ MHz}, 10^\circ)$ and $(148.94 \text{ MHz}, 2^\circ)$, respectively. Lifetimes Γ_B^{-1} (color maps, in units of ms) and binding energy $|E_B|/h$ (contour lines, in units of kHz) for the bound states $\psi_B^{(y)}$ (b) and $\psi_B^{(x)}$ (c).

$(\psi_B^{(+)} - \psi_B^{(-)})$ with distinct critical Rabi frequencies $\Omega_c^{(y)}$ and $\Omega_c^{(x)}$, respectively. Because the wave function of the p_y (p_x)-tetramer state has a larger amplitude along the y (x) direction compared to that along the x (y) direction, we have $\Omega_c^{(y)} \leq \Omega_c \leq \Omega_c^{(x)}$. In Figs. 1(c) and (d), we map out $|\varepsilon_B|$ in the Ω - ξ parameter plane for $\psi_B^{(y)}$ and $\psi_B^{(x)}$, respectively. The dashed lines denote the position of the shape resonance, i.e., the critical Rabi frequencies. As expected, $\Omega_c^{(y)}$ ($\Omega_c^{(x)}$) decreases (increases) with the increase ξ . The dipole moment of tetramer states is approximately twice that for the $|+\rangle$ molecule [62].

Since a tetramer can dissociate into two molecules in the lower six channels, it has a finite lifetime. To determine the lifetimes of the tetramer states, we consider the collisions of two molecules interacting via $V(\mathbf{r})$ with incident energy E_{inc} lying between $E_1^{(\infty)}$ and $E_2^{(\infty)}$ [see Fig. 1(a)]. By tuning incident energy, scattering resonances can be induced when E_{inc} is in resonance with binding energies of the tetramer states. The lifetime of the corresponding tetramer state is associated with the width of the resonance. The above scenario is equivalent to a Feshbach resonance with $\nu = 1$ and $\nu > 1$ being the closed and open channels, respectively. The scattering cross-section in the vicinity of a Feshbach resonance takes the form [63]

$$\sigma(E_{\text{inc}}) = \frac{2\pi}{k_2^2} |ig^2G(E_{\text{inc}}) + S_{\text{bg}} - 1|^2, \quad (5)$$

where $k_2 = \sqrt{2m(E_{\text{inc}} - E_2^{(\infty)})}/\hbar$ is the incident momentum with respect to the channel $|2\rangle$, g is the effective coupling between $|1\rangle$ and $|2\rangle$, and S_{bg} is the background scattering amplitude of molecules in the channel $|2\rangle$. Finally, $G(E) = 1/(E - E_B + i\Gamma_B/2)$ is the propagator describing a transient process that two colliding molecules form a tetramer with binding energy E_B and lifetime $1/\Gamma_B$.

To find the scattering cross section, we perform the coupled-channel scattering calculations which involve all 7 channels [57]. For completeness, we include a van der Waals potential $-C_{\text{vdW}}/r^6$ in $V(\mathbf{r})$ to describe the universal background scattering [64]. Moreover, to account for the loss caused by the formation of the four-body complex, we place an absorption boundary condition inside the shielding core [65]. Figure 2(a) plots the typical cross section σ for the scattering from channel $(\nu lm) = (210)$ to (210) with parameters in the vicinity of the bound state $\psi_B^{(y)}$ (\triangle) and $\psi_B^{(x)}$ (\circ), respectively. The dashed lines are the corresponding fits to Eq. (5), from which one determines the binding energies E_B and decay rate Γ_B . With E_B , we can now calibrate ε_B , i.e., the binding energy obtained via the effective potential. As shown in SM [62], for all control parameters covered by our calculations, the relative difference between ε_B and E_B is always below 10%, which further confirms the validity of the effective potential [57].

In Fig. 2(b) and (c), we map out the lifetime Γ_B^{-1} on the Ω - ξ plane for bound states $\psi_B^{(y)}$ and $\psi_B^{(x)}$, respectively. As a comparison, we also present the corresponding binding energy $|E_B|$ using contour lines. A general observation is that smaller binding energy leads to a larger lifetime. This phenomenon can be roughly understood as follows: A shallower bound state in the closed channel implies a larger incident momentum (or, equivalently, a faster oscillating scattering wave function) in the open channel, which leads to a smaller Frank-Condon factor between closed and open channels. As a result, the decay rate Γ_B becomes smaller. However, a closer look at the contour lines reveals that, even with the same binding energy, the lifetime may vary significantly. For instance, along the contour line with $|E_B|/h = 25 \text{ kHz}$ in Fig. 2(b), the lifetime is extended from 0.4 ms to as large as 24 ms via increasing Ω . Here, a larger Rabi frequency gives rise to a larger energy spacing between asymptotic states of open and closed channels, which effectively improves the shielding effect. Another interesting observation is that the p_x -tetramer state usually has a longer lifetime than its p_y counterpart. This becomes particularly prominent for molecules with larger dipole moments. For example, the lifetime of the p_x -tetramer state of two LiRb molecules can be as long as 10.4 s under suitable control parameters [62, 66]. The sufficiently long lifetime of the tetramers allows one to perform the evaporative

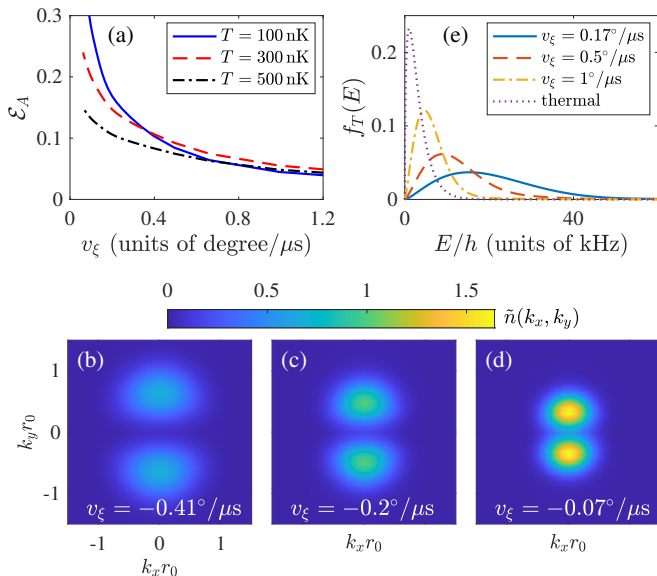


FIG. 3. (a) Ramping rate dependence of the association efficiency for various temperatures with $\Omega/(2\pi) = 150$ MHz and ξ is ramped up from 0.5° to 5° . (b)-(d) Integrated momentum distributions, $\tilde{n}(k_x, k_y)$ (in units of r_0^2), of the dissociated molecules from a tetramer gas with $T = 100$ nK for various ramping rates. (e) Energy distributions $f(E)$ corresponding to (b-d). The dotted line represents the energy distribution of a thermal gas at $T = 100$ nK. For both association and dissociation, ξ is ramped in the range $[0.5^\circ, 5^\circ]$.

cooling of the tetramer gases, which may eventually lead to Bose-Einstein condensations of tetramers.

Association and dissociation of tetramers.—We now turn to study the dynamics of the association and dissociation of the tetramers by using the single-channel model Eq. (3). In general, both association and dissociation can be realized by tuning either ξ or Ω . For simplicity, we shall only present the results for tuning ξ , and the results for varying Ω can be found in SM [62].

To associate a tetramer, we start from a two-molecule scattering state $|\psi_{\mathbf{k}}\rangle$ of relative momentum \mathbf{k} under initial ξ . Then ξ is ramped up with a constant ramp rate $v_\xi \equiv d\xi/dt$ across a shape resonance. The transition probability to the bound state $|\psi_B\rangle$ corresponding to the final ξ is

$$p_a(\mathbf{k}) = |\langle \psi_B | U(\tau) | \psi_{\mathbf{k}} \rangle|^2, \quad (6)$$

where τ is ramp time and $U(\tau) = \mathcal{T} \exp[-i \int_0^\tau dt H_{\text{eff}}(t)]$ is the time-evolution operator with \mathcal{T} denoting the time-ordered exponential. Now, for a molecular gas with density n and temperature T , the *association efficiency* to tetramers can be numerically evaluated using [67, 68]

$$\mathcal{E}_A = 2n\lambda_T^3 \int d\mathbf{k} e^{-\beta k^2/M} p_a(\mathbf{k}), \quad (7)$$

where $\beta = 1/(k_B T)$ is the inverse temperature

with k_B being the Boltzmann constant and $\lambda_T = \sqrt{4\pi\hbar^2/(Mk_B T)}$ is the thermal de Broglie wavelength.

In Fig. 3(a), we plot the v_ξ dependence of \mathcal{E}_A for molecular gases under various temperatures. The association efficiency is a monotonically decreasing function of the ramping rate, indicating that adiabaticity is crucial for achieving higher productivity of tetramers. Interestingly, for the temperature dependence of the conversion efficiency, it is found that \mathcal{E}_A is not a monotonically decreasing function of T , which is somehow in contrast with the intuition since λ_T is a decreasing function of T . A rough explanation is that the thermal distribution should also match $p_a(\mathbf{k})$ to obtain higher \mathcal{E}_A . As a result, \mathcal{E}_A does not necessarily increase as T decreases.

The experimental detection of tetramers can be carried out by first dissociating them into molecules using either RD or MD. For RD, ξ is ramped down to the scattering-state regime with ramping rate v_ξ in a time interval τ . The probability of finding a molecule pair with relative momentum \mathbf{k} is then

$$p_{\text{RD}}(\mathbf{k}) = |\langle \mathbf{k} | U(\tau) | \psi_B \rangle|^2, \quad (8)$$

where $|\psi_B\rangle$ is the bound state corresponding to the initial ξ and $U(\tau)$ is now the time-evolution operator for the dissociation dynamics. Then, for a tetramer gas at equilibrium with temperature T , the momentum distribution of the dissociated molecules is

$$n_T(\mathbf{k}) = \int d\mathbf{p} \frac{e^{-\beta(\mathbf{k}+\mathbf{p})^2/(4M)}}{(4\pi M k_B T)^{3/2}} p_{\text{RD}}\left(\frac{\mathbf{k}-\mathbf{p}}{2}\right), \quad (9)$$

which is experimentally detectable via the time-of-flight (TOF) imaging. In Figs. 3(b-c), we present the integrated momentum distribution, $\tilde{n}_T(k_x, k_y) = \int dk_z n_T(\mathbf{k})$, dissociated from a tetramer gas with $T = 100$ nK at various ramping rates. As can be seen, all momentum distributions are featured by the double peaks, in striking contrast to the narrow crescent shape in the TOF images of MD [46]. Moreover, because the smaller the ramping rate, the higher the visibility, it is more feasible in the experimental detection by adopting smaller ramping rates. We may also distinguish the dissociated molecules by examining their energy distributions, i.e., $f_T(E) = \int d\mathbf{k} \delta(E - k^2/(2M)) n_T(\mathbf{k})$. In Fig. 3(e), we plot the energy distributions of the dissociated molecules corresponding to different ramping rates. As a comparison, we also plot the thermal distribution with $T = 100$ nK. Compared to the thermal gas, $f_T(E)$ of the dissociated molecules is significantly broadened, which can be used as the signature of the tetramer even when the double-peak structure is not observed.

Observations of tetramers are experimentally realized through MD, for which the elliptic angle is periodically modulated around ξ_0 , i.e., $\xi(t) = \xi_0 + \delta\xi \sin \omega_m t$, where $\delta\xi$ and ω_m are the amplitude and frequency of the modulation, respectively. The underlying mechanism of MD is

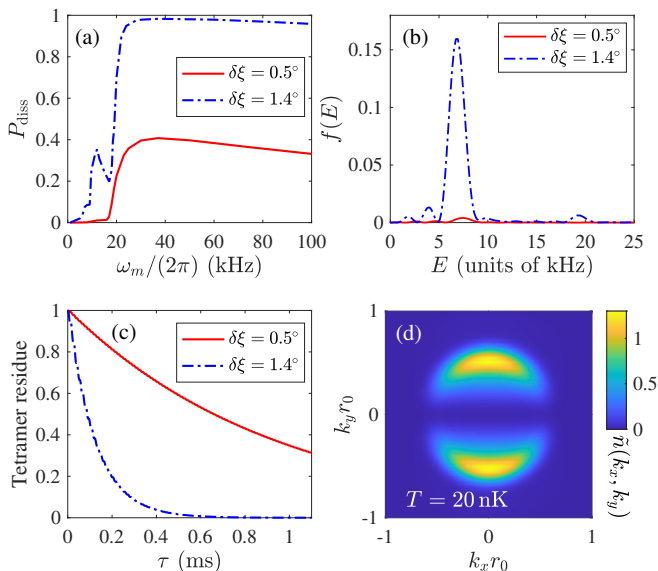


FIG. 4. MD of a p_y tetramer prepared at $\Omega = (2\pi) \times 28.5$ MHz and $\xi_0 = 8^\circ$. The binding energy of the initial state is $|\varepsilon_B|/\hbar = 17$ kHz. (a) P_{diss} versus ω_m for $\tau = 0.5$ ms and different $\delta\xi$'s. (b) Energy distributions of a pair of dissociated molecules with $\omega_m = 2\pi \times 12.5$ kHz, $\tau = 0.5$ ms, and various $\delta\xi$'s. (c) $1 - P_{\text{diss}}$ versus τ at $\omega_m = 2\pi \times 37$ kHz for two $\delta\xi$'s. (d) Integrated momentum distributions for $\omega_m = 2\pi \times 37$ kHz, $\delta\xi = 1.4^\circ$, $\tau = 0.125$ ms, and $T = 20$ nK.

in analogy to the dissociation of Feshbach molecules by modulating the magnetic field [69, 70]. Here we present a detailed analysis. A MD starts with a bound state $|\psi_B\rangle$ prepared under ξ_0 . The *dissociation probability* after being modulated for a driving time τ is $P_{\text{diss}} = \langle \psi(\tau) | \mathcal{P}_{\text{sc}} | \psi(\tau) \rangle$, where $|\psi(\tau)\rangle = U(\tau)|\psi_B\rangle$ with $U(\tau)$ being the time-evolution for MD and $\mathcal{P}_{\text{sc}} = 1 - |\psi_B\rangle\langle\psi_B|$ is a projection operator. The dissociation probability can then be numerically calculated straightforwardly. Interestingly, the dynamics of the system under a small amplitude modulation can be captured by a time-independent Hamiltonian [62].

Figure 4(a) plots the dissociation spectra of a p_y -tetramer state for various $\delta\xi$'s. The binding energy of the initial tetramer is $|\varepsilon_B|/\hbar \simeq 17$ kHz. For $\delta\xi = 0.5^\circ$, P_{diss} first slowly grows with ω_m when ω_m is smaller than the threshold value $\omega_m^* = |\varepsilon_B|/\hbar$. In this regime, the dissociation is mainly due to the off-resonant coupling between the bound state and scattering states. For $\omega_m > \omega_m^*$, the tetramer is resonant to scattering states such that P_{diss} quickly increases and reaches a peak value. Then for $\delta\xi = 1.4^\circ$, although the dissociation spectrum above the threshold only quantitatively differs from that of $\delta\xi = 0.5^\circ$, the below-threshold behavior is completely different. In fact, a dissociation peak emerges at $\omega_m = 2\pi \times 12.5$ kHz, which, as shown below, is due to the multiple-photon excitation under a strong modulation. To show this, let us examine the energy distribution of the disso-

ciated molecules, i.e., $f_0(E) = \int d\mathbf{k} \delta(E - k^2/M) p_{\text{MD}}(\mathbf{k})$, where $p_{\text{MD}}(\mathbf{k}) = |\langle \mathbf{k} | \mathcal{P}_{\text{sc}} | \psi(\tau) \rangle|^2$ is the momentum distribution of two dissociated molecules. Figure 4(b) plots $f_0(E)$ for $\omega_m = 2\pi \times 12.5$ kHz and different $\delta\xi$'s. For $\delta\xi = 1.4^\circ$ a prominent peak at $E/\hbar \approx 2 \times 12.5 - 17 = 8$ kHz is observed, which indicates the dissociation of the tetramer to two molecules after absorbing two photons. Eventually, the two-photon process gives rise to a below-threshold peak on the dissociation spectrum.

Furthermore, we plot, in Fig. 4(c), dissociation probability as a function of driven time for $\omega_m = 2\pi \times 37$ kHz and with two distinct $\delta\xi$'s. In both cases, the dissociation probability decay exponentially as $P_{\text{diss}} = 1 - e^{-\gamma_{\text{diss}}\tau}$, where the dissociation rates are $\gamma_{\text{diss}} = 1.06$ and 8.27 ms^{-1} for $\delta\xi = 0.5^\circ$ and 1.4° , respectively. These results confirm that the above-threshold MD is essentially a spontaneous emission for which the Markovian approximation is valid [62]. Finally, for experimental detection, we consider the momentum distribution of the dissociated molecules from a tetramer gas of temperature T , which can be obtained by replacing $p_{\text{RD}}(\mathbf{k})$ in Eq. (9) by $p_{\text{MD}}(\mathbf{k})$. In Fig. 4(d), we plot the integrated momentum distribution $\tilde{n}_T(k_x, k_y)$ with $T = 20$ nK. As can be seen, the momentum distribution is featured by the crescent shape, in agreement with the experimental observations.

Conclusion.—We have studied the static and dynamic properties of FL tetramers formed by two fermionic MSMs using the effective potential. Our studies reveal that the higher p_x -tetramer states generally exhibit longer lifetimes than the p_y -tetramer states, potentially facilitating further cooling of tetramer gases to quantum degeneracy. Additionally, we propose a novel method for the experimental detection of tetramers by using RD. In the case of MD with large amplitude modulations, we have identified below-threshold peaks in the dissociation spectrum, which are linked to multiple-photon processes. Given the universal form of the inter-molecular potential, our findings are directly applicable to other fermionic molecules, significantly enriching the two- and many-body physics of ultracold molecular gases. Our work opens promising avenues for realizing tetratomic BEC through evaporative cooling and exploring the diverse many-body physics, including the fascinating BCS-BEC crossover in MSMs.

Acknowledgment.—X.-Y. C. and X.-Y. L. thank the MPQ *NaK molecules* team for fruitful discussions. This work was supported by the NSFC (Grants No. 12135018, No.12047503, and No. 12274331), by National Key Research and Development Program of China (Grant No. 2021YFA0718304), and by CAS Project for Young Scientists in Basic Research (Grant No. YSBR-057). X.-Y. C. and X.-Y. L. acknowledge support from the Max Planck Society, the European Union (PASQuaS Grant No. 817482) and the Deutsche Forschungsgemeinschaft under German Excellence Strategy – EXC-2111 – 390814868 and under Grant No. FOR 2247.

* syi@itp.ac.cn

† tshi@itp.ac.cn

- [1] L. D. Carr, D. DeMille, R. V. Krems, and J. Ye, *New Journal of Physics* **11**, 055049 (2009).
- [2] S. Moses, J. Covey, M. Miccnikowski, D. Jin, and J. Ye, *Nature Physics* **13**, 13 (2017).
- [3] C. P. Koch, M. Lemeshko, and D. Sugny, *Rev. Mod. Phys.* **91**, 035005 (2019).
- [4] L. R. Liu, D. Rosenberg, P. B. Changala, P. J. D. Crowley, D. J. Nesbitt, N. Y. Yao, T. Tscherbul, and J. Ye, *Science* **381**, 778 (2023).
- [5] R. V. Krems, *Phys Chem Chem Phys* **10**, 4079 (2008).
- [6] M.-G. Hu, Y. Liu, D. D. Grimes, Y.-W. Lin, A. H. Gheorghe, R. Vexiau, N. Bouloufa-Maafa, O. Dulieu, T. Rosenband, and K.-K. Ni, *Science* **366**, 1111 (2019), <https://www.science.org/doi/pdf/10.1126/science.aay9531>.
- [7] Y. Liu and K.-K. Ni, *Annu. Rev. Phys. Chem.* **73**, 73 (2022).
- [8] D. DeMille, *Phys. Rev. Lett.* **88**, 067901 (2002).
- [9] R. Sawant, J. A. Blackmore, P. D. Gregory, J. Mur-Petit, D. Jaksch, J. Aldegunde, J. M. Hutson, M. R. Tarbutt, and S. L. Cornish, *New Journal of Physics* **22**, 013027 (2020).
- [10] A. Micheli, G. K. Brennen, and P. Zoller, *Nature Physics* **2**, 341 (2006).
- [11] E. Altman, K. R. Brown, G. Carleo, L. D. Carr, E. Demler, C. Chin, B. DeMarco, S. E. Economou, M. A. Eriksson, K.-M. C. Fu, M. Greiner, K. R. Hazzard, R. G. Hulet, A. J. Kollár, B. L. Lev, M. D. Lukin, R. Ma, X. Mi, S. Misra, C. Monroe, K. Murch, Z. Nazario, K.-K. Ni, A. C. Potter, P. Roushan, M. Saffman, M. Schleier-Smith, I. Siddiqi, R. Simmonds, M. Singh, I. Spielman, K. Temme, D. S. Weiss, J. Vučković, V. Vuletić, J. Ye, and M. Zwierlein, *PRX Quantum* **2**, 017003 (2021).
- [12] P. Rabl, D. DeMille, J. M. Doyle, M. D. Lukin, R. J. Schoelkopf, and P. Zoller, *Phys. Rev. Lett.* **97**, 033003 (2006).
- [13] C. M. Tesch and R. de Vivie-Riedle, *Phys. Rev. Lett.* **89**, 157901 (2002).
- [14] M. L. Wall, K. Maeda, and L. D. Carr, *New J. Phys.* **17**, 025001 (2015).
- [15] V. V. Albert, J. P. Covey, and J. Preskill, *Phys. Rev. X* **10**, 031050 (2020).
- [16] V. V. Flambaum and M. G. Kozlov, *Phys. Rev. Lett.* **99**, 150801 (2007).
- [17] T. A. Isaev, S. Hoekstra, and R. Berger, *Phys. Rev. A* **82**, 052521 (2010).
- [18] J. J. Hudson, D. M. Kara, I. J. Smallman, B. E. Sauer, M. R. Tarbutt, and E. A. Hinds, *Nature* **473**, 493 (2011).
- [19] N. R. Hutzler, *Quantum Sci. Technol.* **5**, 044011 (2020).
- [20] K.-K. Ni, S. Ospelkaus, M. H. G. de Miranda, A. Pe'er, B. Neyenhuis, J. J. Zirbel, S. Kotochigova, P. S. Julienne, D. S. Jin, and J. Ye, *Science* **322**, 231 (2008), <https://www.science.org/doi/pdf/10.1126/science.1163861>.
- [21] T. Takekoshi, L. Reichsöllner, A. Schindewolf, J. M. Hutson, C. R. Le Sueur, O. Dulieu, F. Ferlaino, R. Grimm, and H.-C. Nägerl, *Phys. Rev. Lett.* **113**, 205301 (2014).
- [22] T. Takekoshi, L. Reichsöllner, A. Schindewolf, J. M. Hutson, C. R. Le Sueur, O. Dulieu, F. Ferlaino, R. Grimm, and H.-C. Nägerl, *Phys. Rev. Lett.* **113**, 205301 (2014).
- [23] J. W. Park, S. A. Will, and M. W. Zwierlein, *Phys. Rev. Lett.* **114**, 205302 (2015).
- [24] F. Seeßelberg, N. Buchheim, Z.-K. Lu, T. Schneider, X.-Y. Luo, E. Tiemann, I. Bloch, and C. Gohle, *Phys. Rev. A* **97**, 013405 (2018).
- [25] K. K. Voges, P. Gersema, M. Meyer zum Alten Borgloh, T. A. Schulze, T. Hartmann, A. Zenesini, and S. Ospelkaus, *Phys. Rev. Lett.* **125**, 083401 (2020).
- [26] M. Guo, B. Zhu, B. Lu, X. Ye, F. Wang, R. Vexiau, N. Bouloufa-Maafa, G. Quéméner, O. Dulieu, and D. Wang, *Phys. Rev. Lett.* **116**, 205303 (2016).
- [27] T. M. Rvachov, H. Son, A. T. Sommer, S. Ebadi, J. J. Park, M. W. Zwierlein, W. Ketterle, and A. O. Jamison, *Phys. Rev. Lett.* **119**, 143001 (2017).
- [28] I. Stevenson, A. Z. Lam, N. Bigagli, C. Warner, W. Yuan, S. Zhang, and S. Will, *Phys. Rev. Lett.* **130**, 113002 (2023).
- [29] W. B. Cairncross, J. T. Zhang, L. R. B. Picard, Y. Yu, K. Wang, and K.-K. Ni, *Phys. Rev. Lett.* **126**, 123402 (2021).
- [30] N. Fitch and M. Tarbutt (Academic Press, 2021) pp. 157–262.
- [31] G. Valtolina, K. Matsuda, W. G. Tobias, J.-R. Li, L. De Marco, and J. Ye, *Nature* **588**, 239 (2020).
- [32] J.-R. Li, W. G. Tobias, K. Matsuda, C. Miller, G. Valtolina, L. De Marco, R. R. W. Wang, L. Lassablière, G. Quéméner, J. L. Bohn, and J. Ye, *Nature Physics* **17**, 1144 (2021).
- [33] K. Matsuda, L. D. Marco, J.-R. Li, W. G. Tobias, G. Valtolina, G. Quéméner, and J. Ye, *Science* **370**, 1324 (2020), <https://www.science.org/doi/pdf/10.1126/science.abe7370>.
- [34] L. Anderegg, S. Burchesky, Y. Bao, S. S. Yu, T. Karman, E. Chae, K.-K. Ni, W. Ketterle, and J. M. Doyle, *Science* **373**, 779 (2021), <https://www.science.org/doi/pdf/10.1126/science.abg9502>.
- [35] L. D. Marco, G. Valtolina, K. Matsuda, W. G. Tobias, J. P. Covey, and J. Ye, *Science* **363**, 853 (2019), <https://www.science.org/doi/pdf/10.1126/science.aau7230>.
- [36] M. Duda, X.-Y. Chen, A. Schindewolf, R. Bause, J. von Milczewski, R. Schmidt, I. Bloch, and X.-Y. Luo, *Nat. Phys.* **19**, 720 (2023).
- [37] A. Schindewolf, R. Bause, X.-Y. Chen, M. Duda, T. Karman, I. Bloch, and X.-Y. Luo, *Nature* **607**, 677 (2022).
- [38] X.-Y. Chen, A. Schindewolf, S. Eppelt, R. Bause, M. Duda, S. Biswas, T. Karman, T. Hilker, I. Bloch, and X.-Y. Luo, *Nature* **614**, 59 (2022).
- [39] J. Cao, H. Yang, Z. Su, X.-Y. Wang, J. Rui, B. Zhao, and J.-W. Pan, *Phys. Rev. A* **107**, 013307 (2023).
- [40] J. Lin, G. Chen, M. Jin, Z. Shi, F. Deng, W. Zhang, G. Quéméner, T. Shi, S. Yi, and D. Wang, *Phys. Rev. X* **13**, 031032 (2023).
- [41] N. Bigagli, C. Warner, W. Yuan, S. Zhang, I. Stevenson, T. Karman, and S. Will, *Nat. Phys.* **19**, 1579 (2023).
- [42] N. Bigagli, W. Yuan, S. Zhang, B. Bulatovic, T. Karman, I. Stevenson, and S. Will, “Observation of bose-einstein condensation of dipolar molecules,” (2023), [arXiv:2312.10965 \[cond-mat.quant-gas\]](https://arxiv.org/abs/2312.10965).
- [43] L. Lassablière and G. Quéméner, *Phys. Rev. Lett.* **121**, 163402 (2018).
- [44] J. J. Park, Y.-K. Lu, A. O. Jamison, T. V. Tscherbul, and W. Ketterle, *Nature* **614**, 54 (2023).
- [45] G. Tang, M. Besemer, S. Kuijpers, G. C. Groenenboom, A. van der Avoird, T. Karman, and S. Y. T. van de Meerakker, *Science* **379**, 1031 (2023).

- [46] X.-Y. Chen, S. Biswas, S. Eppelt, A. Schindewolf, F. Deng, T. Shi, S. Yi, T. A. Hilker, I. Bloch, and X.-Y. Luo, *Nature* **626**, 283 (2024).
- [47] T. Lahaye, C. Menotti, L. Santos, M. Lewenstein, and T. Pfau, *Reports on Progress in Physics* **72**, 126401 (2009).
- [48] L. You and M. Marinescu, *Phys. Rev. A* **60**, 2324 (1999).
- [49] M. A. Baranov, M. S. Mar'enko, V. S. Rychkov, and G. V. Shlyapnikov, *Phys. Rev. A* **66**, 013606 (2002).
- [50] T. Shi, J.-N. Zhang, C.-P. Sun, and S. Yi, *Phys. Rev. A* **82**, 033623 (2010).
- [51] C. Zhao, L. Jiang, X. Liu, W. M. Liu, X. Zou, and H. Pu, *Phys. Rev. A* **81**, 063642 (2010).
- [52] C. Wu and J. E. Hirsch, *Phys. Rev. B* **81**, 020508 (2010).
- [53] J. Levinsen, N. R. Cooper, and G. V. Shlyapnikov, *Phys. Rev. A* **84**, 013603 (2011).
- [54] M. A. Baranov, M. Dalmonte, G. Pupillo, and P. Zoller, *Chem Rev* **112**, 5012 (2012).
- [55] T. Shi, S.-H. Zou, H. Hu, C.-P. Sun, and S. Yi, *Phys. Rev. Lett.* **110**, 045301 (2013).
- [56] R. Qi, Z.-Y. Shi, and H. Zhai, *Phys. Rev. Lett.* **110**, 045302 (2013).
- [57] F. Deng, X.-Y. Chen, X.-Y. Luo, W. Zhang, S. Yi, and T. Shi, *Phys. Rev. Lett.* **130**, 183001 (2023).
- [58] G. Quéméner, J. L. Bohn, and J. F. E. Croft, *Phys. Rev. Lett.* **131**, 043402 (2023).
- [59] R. Bause, A. Christianen, A. Schindewolf, I. Bloch, and X.-Y. Luo, *J. Phys. Chem. A* **127**, 729 (2023).
- [60] C. A. R. Sá de Melo, M. Randeria, and J. R. Engelbrecht, *Phys. Rev. Lett.* **71**, 3202 (1993).
- [61] M. Iskin and C. A. R. Sá de Melo, *Phys. Rev. Lett.* **96**, 040402 (2006).
- [62] See Supplemental Material for a detailed derivation of the effective potential, the numerical procedure for the scattering calculation, and the effective potential in the momentum space.
- [63] J. R. Taylor, Scattering Theory The Quantum Theory of Nonrelativistic Collisions (John Wiley & Sons, Inc., New York, 1972).
- [64] Z. Idziaszek and P. S. Julienne, *Phys. Rev. Lett.* **104**, 113202 (2010).
- [65] D. C. Clary and J. P. Henshaw, *Faraday Discuss. Chem. Soc.* **84**, 333 (1987).
- [66] M. Aymar and O. Dulieu, *J. Chem. Phys.* **122**, 204302 (2005).
- [67] T. M. Hanna, T. Köhler, and K. Burnett, *Phys. Rev. A* **75**, 013606 (2007).
- [68] P. Giannakeas, L. Khaykovich, J.-M. Rost, and C. H. Greene, *Phys. Rev. Lett.* **123**, 043204 (2019).
- [69] C. Chin and P. S. Julienne, *Phys. Rev. A* **71**, 012713 (2005).
- [70] Z. Guo, F. Jia, B. Zhu, L. Li, J. M. Hutson, and D. Wang, *Phys. Rev. A* **105**, 023313 (2022).
- [71] H. Bachau, E. Cormier, P. Decleva, J. E. Hansen, and F. Martín, *Reports on Progress in Physics* **64**, 1815 (2001).
- [72] B. Johnson, *Journal of Computational Physics* **13**, 445 (1973).
- [73] E. J. Rackham, T. Gonzalez-Lezana, and D. E. Manolopoulos, *The Journal of Chemical Physics* **119**, 12895 (2003), https://pubs.aip.org/aip/jcp/article-pdf/119/24/12895/19253314/12895.1_online.pdf.
- [74] J. E. Williams, N. Nygaard, and C. W. Clark, *New Journal of Physics* **8**, 150 (2006).

Supplemental Materials:

This Supplemental Material is structured as follows. In the first section, we derive the effective potential V_{eff} for two molecules in the highest dressed state channel and dipole moments of tetramers. In the second section, we employ the log-derivative method to calculate scattering amplitudes, cross sections, the binding energies and the life-time of tetramers using the 7 channel model, where the validity of V_{eff} is justified. In the third section, we calculate the association efficiency and the momentum (energy) distribution in the ramp dissociation. In the fourth section, we derive the effective Hamiltonian describing the modulational dissociation. In the fifth section, we calculate the dissociation spectrum and the momentum distribution in the modulational dissociation.

S1. GENERIC EFFECTIVE POTENTIALS FOR MICROWAVE SHIELDED MOLECULES

In the section, we derive an effective potential for microwave shielded molecules. We focus on four lowest rotational states ($|J, M_J\rangle = |0, 0\rangle, |1, 0\rangle, \text{ and } |1, \pm 1\rangle$) of the molecule, where the electric dipole moment of a molecule is $d\hat{\mathbf{d}}$ with $\hat{\mathbf{d}}$ being the unit vector along the internuclear axis of the molecule. A position-independent elliptically polarized microwave field propagating along the z axis induces the transition between the rotational ground state $|0, 0\rangle$ and the excited state $|\xi_+\rangle \equiv \cos \xi |1, 1\rangle + \sin \xi |1, -1\rangle$, where ξ is the elliptic angle. In the interaction picture, the single-particle Hamiltonian reads

$$\hat{h}_{\text{in}} = \delta \sum_{M_J} |1, M_J\rangle \langle 1, M_J| + \frac{\Omega}{2} (|\xi_+\rangle \langle 0, 0| + \text{H.c.}), \quad (\text{S1})$$

where $\delta = \omega_1 - \omega_0$ is the detuning between the energy level spacing ω_1 and the microwave frequency ω_0 , and Ω is the Rabi frequency. The eigenstates of \hat{h}_{in} are $|0\rangle \equiv |1, 0\rangle$, $|\xi_-\rangle \equiv \cos \xi |1, -1\rangle - \sin \xi |1, 1\rangle$, $|+\rangle \equiv u|0, 0\rangle + v|\xi_+\rangle$, and $|-\rangle \equiv u|\xi_+\rangle - v|0, 0\rangle$, where $u = \sqrt{(1 - \delta/\Omega_{\text{eff}})/2}$, $v = \sqrt{(1 + \delta/\Omega_{\text{eff}})/2}$, and $\Omega_{\text{eff}} = \sqrt{\delta^2 + \Omega^2}$ is the effective Rabi frequency. The corresponding eigenenergies are $E_0 = E_{\xi_-} = \delta$ and $E_{\pm} = (\delta \pm \Omega_{\text{eff}})/2$.

In the center of mass frame, the two-body Hamiltonian is $H = -\nabla^2/M + V(\mathbf{r})$, where \mathbf{r} is the relative coordinate. The interaction potential $V(\mathbf{r}) = V_{\text{in}} - C_{\text{vdW}}/r^6$ contains the internal-state dependent part $V_{\text{in}} = \sum_{j=1,2} \hat{h}_{\text{in},j} + V_{\text{dd}}(\mathbf{r})$ and the universal van der Waals interaction described by C_{vdW} , where

$$\begin{aligned} V_{\text{dd}}(\mathbf{r}) &= \frac{d^2}{4\pi\epsilon_0 r^3} \left[\hat{\mathbf{d}}_1 \cdot \hat{\mathbf{d}}_2 - 3(\hat{\mathbf{d}}_1 \cdot \hat{\mathbf{r}})(\hat{\mathbf{d}}_2 \cdot \hat{\mathbf{r}}) \right] \\ &= -8\sqrt{\frac{2}{15}}\pi^{3/2} \frac{d^2}{4\pi\epsilon_0 r^3} \sum_{m=-2}^2 Y_{2m}^*(\hat{\mathbf{r}}) \Sigma_{2,m} \end{aligned} \quad (\text{S2})$$

is the dipolar interaction of molecules and $Y_{2m}(\hat{\mathbf{r}})$ are spherical harmonics. The rank-2 spherical tensor Σ_2 with components

$$\Sigma_{2,0} = \frac{1}{\sqrt{6}}(\hat{d}_1^+ \hat{d}_2^- + \hat{d}_1^- \hat{d}_2^+ + 2\hat{d}_1^0 \hat{d}_2^0), \quad \Sigma_{2,\pm 1} = \frac{1}{\sqrt{2}}(\hat{d}_1^\pm \hat{d}_2^0 + \hat{d}_1^0 \hat{d}_2^\pm), \quad \text{and } \Sigma_{2,\pm 2} = \hat{d}_1^\pm \hat{d}_2^\pm \quad (\text{S3})$$

is determined by $\hat{d}_j^\pm = Y_{1,\pm 1}(\hat{\mathbf{d}}_j)$ and $\hat{d}_j^0 = Y_{1,0}(\hat{\mathbf{d}}_j)$ with $\hat{\mathbf{d}}_{j=1,2}$ being the unit vector along the directions of the j th dipole moment. In the basis $|J, M_J\rangle$,

$$\hat{d}^0 = \hat{d}_p^0 e^{-i\omega_0 t} + \hat{d}_p^{0\dagger} e^{i\omega_0 t}, \quad \hat{d}^+ = \hat{d}_p^+ e^{-i\omega_0 t} + \hat{d}_m^+ e^{i\omega_0 t}, \quad \text{and } \hat{d}^- = -(\hat{d}^+)^\dagger, \quad (\text{S4})$$

where $\hat{d}_p^0 = |0, 0\rangle \langle 1, 0|/\sqrt{4\pi}$ and $\hat{d}_p^\pm = -|0, 0\rangle \langle 1, -1|/\sqrt{4\pi}$ are the positive frequency parts, and $\hat{d}_m^\pm = |1, 1\rangle \langle 0, 0|/\sqrt{4\pi}$ is the negative frequency part.

For convenient, we study the scattering in the dressed-state basis $\{|+\rangle, |0\rangle, |\xi_-\rangle, |-\rangle\}$, i.e., the eigenbasis of $\hat{h}_{\text{in},j}$. We focus on the microwave shielding effect of two molecules in the highest dressed state $|1\rangle = |+, +\rangle$. It turns out that $V(\mathbf{r})$ only couples $|1\rangle$ to other six states $|2\rangle = |+, 0\rangle_s$, $|3\rangle = |+, \xi_-\rangle_s$, $|4\rangle = |+, -\rangle_s$, $|5\rangle = |-, 0\rangle_s$, $|6\rangle = |-, \xi_-\rangle_s$, and $|7\rangle = |-, -\rangle$ in the symmetric subspace, where $|i, j\rangle_s = (|i, j\rangle + |j, i\rangle)/\sqrt{2}$. Projecting $V(\mathbf{r})$ in the subspace $\mathcal{S}_7 = \{|\nu\rangle\}_{\nu=1}^7$, we obtain the potential

$$V_{\nu\nu'}(\mathbf{r}) = (\mathcal{E}_\nu - \frac{C_{\text{vdW}}}{r^6})\delta_{\nu\nu'} - 8\sqrt{\frac{2}{15}}\pi^{3/2} \frac{d^2}{4\pi\epsilon_0 r^3} \sum_{m=-2}^2 Y_{2m}^*(\hat{\mathbf{r}}) (\Sigma_{2,m})_{\nu\nu'}, \quad (\text{S5})$$

where the asymptotic energy

$$\mathcal{E} = \begin{pmatrix} 0 & 0 & 0 & 0 & 0 & 0 & 0 \\ 0 & \frac{1}{2}(\delta - \Omega_{\text{eff}}) & 0 & 0 & 0 & 0 & 0 \\ 0 & 0 & \frac{1}{2}(\delta - \Omega_{\text{eff}}) & 0 & 0 & 0 & 0 \\ 0 & 0 & 0 & -\Omega_{\text{eff}} & 0 & 0 & 0 \\ 0 & 0 & 0 & 0 & \frac{1}{2}(\delta - 3\Omega_{\text{eff}}) & 0 & 0 \\ 0 & 0 & 0 & 0 & 0 & \frac{1}{2}(\delta - 3\Omega_{\text{eff}}) & 0 \\ 0 & 0 & 0 & 0 & 0 & 0 & -2\Omega_{\text{eff}} \end{pmatrix} \quad (\text{S6})$$

is defined with respect to the highest channel. The spherical tensor Σ_2 in the space \mathcal{S}_7 becomes

$$\begin{aligned} \Sigma_{2,0} &= \frac{1}{4\pi\sqrt{6}} \begin{pmatrix} -2u^2v^2 & 0 & 0 & -\sqrt{2}uvw & 0 & 0 & 2u^2v^2 \\ 0 & 2u^2 & 0 & 0 & -2uv & 0 & 0 \\ 0 & 0 & -u^2 & 0 & 0 & uv & 0 \\ -\sqrt{2}uvw & 0 & 0 & -w^2 & 0 & 0 & \sqrt{2}uvw \\ 0 & -2uv & 0 & 0 & 2v^2 & 0 & 0 \\ 0 & 0 & uv & 0 & 0 & -v^2 & 0 \\ 2u^2v^2 & 0 & 0 & \sqrt{2}uvw & 0 & 0 & -2u^2v^2 \end{pmatrix}, \\ \Sigma_{2,1} &= \frac{1}{4\pi\sqrt{2}} \begin{pmatrix} 0 & \sqrt{2}u^2v \cos \xi & 0 & 0 & -\sqrt{2}uv^2 \cos \xi & 0 & 0 \\ -\sqrt{2}u^2v \sin \xi & 0 & -u^2 \cos \xi & -uv \sin \xi & 0 & uv \cos \xi & \sqrt{2}u^2v \sin \xi \\ 0 & -u^2 \sin \xi & 0 & 0 & uv \sin \xi & 0 & 0 \\ 0 & uv \cos \xi & 0 & 0 & -vw \cos \xi & 0 & 0 \\ \sqrt{2}uv^2 \sin \xi & 0 & uv \cos \xi & vw \sin \xi & 0 & -v^2 \cos \xi & -\sqrt{2}uv^2 \sin \xi \\ 0 & uv \sin \xi & 0 & 0 & -v^2 \sin \xi & 0 & 0 \\ 0 & -\sqrt{2}u^2v \cos \xi & 0 & 0 & \sqrt{2}uv^2 \cos \xi & 0 & 0 \end{pmatrix}, \\ \Sigma_{2,2} &= -\frac{1}{4\pi} \begin{pmatrix} u^2v^2 \sin 2\xi & 0 & \sqrt{2}u^2v \cos^2 \xi & \frac{\sqrt{2}}{2}uvw \sin 2\xi & 0 & -\sqrt{2}uv^2 \cos^2 \xi & -u^2v^2 \sin 2\xi \\ 0 & 0 & 0 & 0 & 0 & 0 & 0 \\ -\sqrt{2}u^2v \sin^2 \xi & 0 & -\frac{1}{2}u^2 \sin 2\xi & -uv \sin^2 \xi & 0 & \frac{1}{2}uv \sin 2\xi & \sqrt{2}u^2v \sin^2 \xi \\ \frac{\sqrt{2}}{2}uvw \sin 2\xi & 0 & uv \cos^2 \xi & \frac{1}{2}w^2 \sin 2\xi & 0 & -vw \cos^2 \xi & -\frac{\sqrt{2}}{2}uvw \sin 2\xi \\ 0 & 0 & 0 & 0 & 0 & 0 & 0 \\ \sqrt{2}uv^2 \sin^2 \xi & 0 & \frac{1}{2}uv \sin 2\xi & vw \sin^2 \xi & 0 & -\frac{1}{2}v^2 \sin 2\xi & -\sqrt{2}uv^2 \sin^2 \xi \\ -u^2v^2 \sin 2\xi & 0 & -\sqrt{2}u^2v \cos^2 \xi & -\frac{\sqrt{2}}{2}uvw \sin 2\xi & 0 & \sqrt{2}uv^2 \cos^2 \xi & u^2v^2 \sin 2\xi \end{pmatrix}, \quad (\text{S7}) \end{aligned}$$

where $w = u^2 - v^2$.

The adiabatic potential of the highest channel can be obtained by diagonalizing the 7×7 matrix $V_{\nu\nu'}(\mathbf{r})$ for all \mathbf{r} . The largest eigenvalue $V_{\text{adia}}(\mathbf{r})$ gives rise to the effective potential for two incident molecules in the state $|1\rangle$. The corresponding position dependent eigen-vector $|1(\mathbf{r})\rangle = \sum_{\nu} \alpha_{\nu}(\mathbf{r})|\nu\rangle$ describes the mixing of the seven bare channels induced by the dipolar interaction, where $\alpha_{\nu}(\mathbf{r} \rightarrow \infty) = (1, 0, 0, 0, 0, 0, 0)^T$. For the low energy scattering, the second order perturbation leads to the effective potential $V_{\text{adia}}(\mathbf{r}) \sim V_{\text{eff}}(\mathbf{r})$:

$$\begin{aligned} V_{\text{eff}}(\mathbf{r}) &= \frac{C_6}{r^6} \sin^2 \theta \{1 - \mathcal{F}_{\xi}^2(\varphi) + [1 - \mathcal{F}_{\xi}(\varphi)]^2 \cos^2 \theta\} \\ &\quad + \frac{C_3}{r^3} [3 \cos^2 \theta - 1 + 3\mathcal{F}_{\xi}(\varphi) \sin^2 \theta] - \frac{C_{\text{vdW}}}{r^6}, \quad (\text{S8}) \end{aligned}$$

where $\mathcal{F}_{\xi}(\varphi) = \sin 2\xi \cos 2\varphi$, θ and φ are the polar and azimuthal angles of \mathbf{r} . The strength $C_3 = d^2 / [48\pi\epsilon_0(1 + \delta_r^2)]$ of the long range DDI only depends on the relative detuning $\delta_r = |\delta|/\Omega$, and $C_6 > 0$ is obtained by fitting with the adiabatic potential V_{adia} .

Since the shielding core around $10^2 \sim 10^3 a_0$ generated by the C_6 potential is much larger than the range of the van der Waals potential, two shielded molecules in the tetramer bound state with distance $10^2 \sim 10^3 a_0$ barely feel the van der Waals potential. Therefore, we study the binding energy of the tetramer state by neglecting the van der Waals C_{vdW} -term. However, we note that the C_{vdW} -term has the effect on the formation of the four body complex inside the shielding core, thus, the life-time of the tetramer state is calculated by taking into account the van der Waals potential. Using the B-spline algorithm [S71], we numerically solve the Schrödinger equation (SE)

$$\left[-\frac{\nabla^2}{M} + V_{\text{eff}}(\mathbf{r})\right]\psi_B(\mathbf{r}) = \varepsilon_B \psi_B(\mathbf{r}) \quad (\text{S9})$$

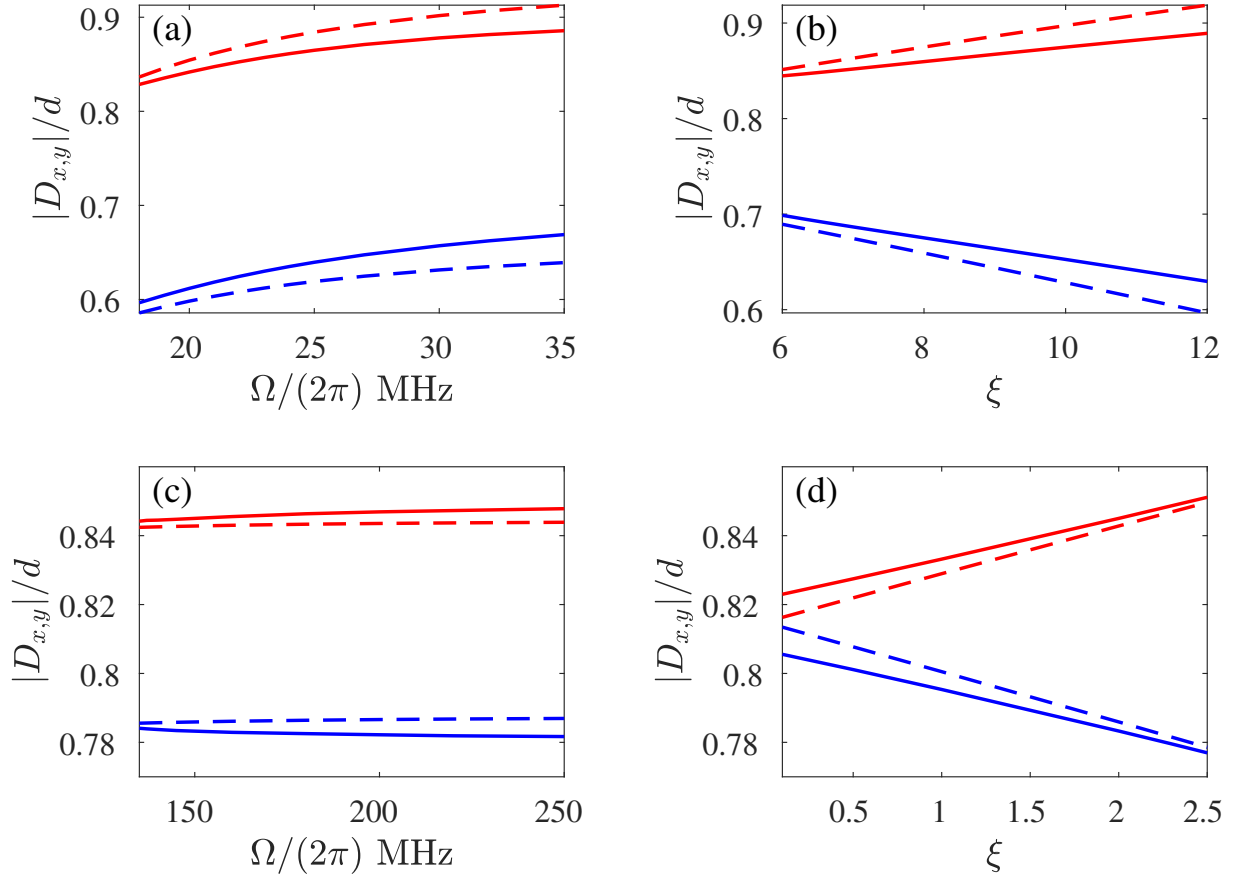


FIG. S1. Dipole moments $|D_{x,y}|$ of the p_y - and p_x -tetramer states are shown in the first and second rows, respectively, where $\delta/(2\pi) = -9.5\text{MHz}$. The solid blue and red curves represent $|D_x|$ and $|D_y|$, while the dashed blue and red curves show the dipole moments $|D_{\text{tot},x}|$ and $|D_{\text{tot},y}|$ of two widely separated molecules. (a) $\xi = 10^\circ$; (b) $\Omega/(2\pi) = 28.5\text{MHz}$; (c) $\xi = 2^\circ$; (d) $\Omega/(2\pi) = 150\text{MHz}$.

to determine the tetramer wavefunction $\psi_B(\mathbf{r})$ and the binding energy $|\varepsilon_B|$.

In the seven bare dressed-state basis, the tetramer state is $\Psi_B(\mathbf{r}) = \sum_\nu \psi_B(\mathbf{r})\alpha_\nu(\mathbf{r})|\nu\rangle$. The dipole moment of the tetramer is $\mathbf{D} = d \sum_{j=1,2} \int d\mathbf{r} \Psi_B^\dagger(\mathbf{r}) \hat{\mathbf{d}}_j \Psi_B(\mathbf{r})$. In the explicit form,

$$\begin{aligned} \mathbf{D}^z &= 4d\sqrt{\frac{\pi}{3}} \sum_{j=1,2} \text{Re} \langle \hat{d}_{p,j}^0 \rangle e^{-i\omega_0 t}, \\ \mathbf{D}^x &= -2d\sqrt{\frac{2\pi}{3}} \sum_{j=1,2} \text{Re}(\langle \hat{d}_{p,j}^+ \rangle + \langle \hat{d}_{m,j}^{+\dagger} \rangle) e^{-i\omega_0 t} \\ &= -2d\sqrt{\frac{2\pi}{3}} \sum_{j=1,2} [\text{Re}(\langle \hat{d}_{p,j}^+ \rangle + \langle \hat{d}_{m,j}^+ \rangle) \cos \omega_0 t + \text{Im}(\langle \hat{d}_{p,j}^+ \rangle - \langle \hat{d}_{m,j}^+ \rangle) \sin \omega_0 t] \end{aligned} \quad (\text{S10})$$

$$\begin{aligned} \mathbf{D}^y &= 2d\sqrt{\frac{2\pi}{3}} \sum_{j=1,2} \text{Re}i(\langle \hat{d}_{p,j}^+ \rangle - \langle \hat{d}_{m,j}^{+\dagger} \rangle) e^{-i\omega_0 t} \\ &= -2d\sqrt{\frac{2\pi}{3}} \sum_{j=1,2} [\text{Im}(\langle \hat{d}_{p,j}^+ \rangle + \langle \hat{d}_{m,j}^+ \rangle) \cos \omega_0 t - \text{Re}(\langle \hat{d}_{p,j}^+ \rangle - \langle \hat{d}_{m,j}^+ \rangle) \sin \omega_0 t] \end{aligned} \quad (\text{S11})$$

where the average value is defined as

$$\langle O \rangle = \int d\mathbf{r} |\psi_B(\mathbf{r})|^2 \sum_{\nu\nu'} \alpha_{\nu'}^*(\mathbf{r}) \langle \nu' | O | \nu \rangle \alpha_\nu(\mathbf{r}). \quad (\text{S12})$$

Since \mathcal{S}_7 is the symmetric subspace, we only have to calculate the average values for one molecule. For instance, the matrices for the molecule $j = 1$ are

$$\begin{aligned}
\hat{d}_{p,1}^0 &= \frac{1}{2\sqrt{2\pi}} \begin{pmatrix} 0 & u & 0 & 0 & 0 & 0 & 0 \\ 0 & 0 & 0 & 0 & 0 & 0 & 0 \\ 0 & 0 & 0 & 0 & 0 & 0 & 0 \\ 0 & -\frac{v}{\sqrt{2}} & 0 & 0 & \frac{u}{\sqrt{2}} & 0 & 0 \\ 0 & 0 & 0 & 0 & 0 & 0 & 0 \\ 0 & 0 & 0 & 0 & 0 & 0 & 0 \\ 0 & 0 & 0 & 0 & -v & 0 & 0 \end{pmatrix}, \\
\hat{d}_{p,1}^+ &= \begin{pmatrix} -\frac{uv \sin \xi}{2\sqrt{\pi}} & 0 & -\frac{u \cos \xi}{2\sqrt{2\pi}} & -\frac{u^2 \sin \xi}{2\sqrt{2\pi}} & 0 & 0 & 0 \\ 0 & -\frac{uv \sin \xi}{4\sqrt{\pi}} & 0 & 0 & -\frac{u^2 \sin \xi}{4\sqrt{\pi}} & 0 & 0 \\ 0 & 0 & -\frac{uv \sin \xi}{4\sqrt{\pi}} & 0 & 0 & -\frac{u^2 \sin \xi}{4\sqrt{\pi}} & 0 \\ \frac{v^2 \sin \xi}{2\sqrt{2\pi}} & 0 & \frac{v \cos \xi}{4\sqrt{\pi}} & 0 & 0 & -\frac{u \cos \xi}{4\sqrt{\pi}} & -\frac{u^2 \sin \xi}{2\sqrt{2\pi}} \\ 0 & \frac{v^2 \sin \xi}{4\sqrt{\pi}} & 0 & 0 & \frac{uv \sin \xi}{4\sqrt{\pi}} & 0 & 0 \\ 0 & 0 & \frac{v^2 \sin \xi}{4\sqrt{\pi}} & 0 & 0 & \frac{uv \sin \xi}{4\sqrt{\pi}} & 0 \\ 0 & 0 & 0 & \frac{v^2 \sin \xi}{2\sqrt{2\pi}} & 0 & \frac{v \cos \xi}{2\sqrt{2\pi}} & \frac{uv \sin \xi}{2\sqrt{\pi}} \end{pmatrix}, \\
\hat{d}_{m,1}^+ &= \begin{pmatrix} \frac{uv \cos \xi}{2\sqrt{\pi}} & 0 & 0 & -\frac{v^2 \cos \xi}{2\sqrt{2\pi}} & 0 & 0 & 0 \\ 0 & \frac{uv \cos \xi}{4\sqrt{\pi}} & 0 & 0 & -\frac{v^2 \cos \xi}{4\sqrt{\pi}} & 0 & 0 \\ -\frac{u \sin \xi}{2\sqrt{2\pi}} & 0 & \frac{uv \cos \xi}{4\sqrt{\pi}} & \frac{v \sin \xi}{4\sqrt{\pi}} & 0 & -\frac{v^2 \cos \xi}{4\sqrt{\pi}} & 0 \\ \frac{u^2 \cos \xi}{2\sqrt{2\pi}} & 0 & 0 & 0 & 0 & 0 & -\frac{v^2 \cos \xi}{2\sqrt{2\pi}} \\ 0 & \frac{u^2 \cos \xi}{4\sqrt{\pi}} & 0 & 0 & -\frac{uv \cos \xi}{4\sqrt{\pi}} & 0 & 0 \\ 0 & 0 & \frac{u^2 \cos \xi}{4\sqrt{\pi}} & -\frac{u \sin \xi}{4\sqrt{\pi}} & 0 & -\frac{uv \cos \xi}{4\sqrt{\pi}} & \frac{v \sin \xi}{2\sqrt{2\pi}} \\ 0 & 0 & 0 & \frac{u^2 \cos \xi}{2\sqrt{2\pi}} & 0 & 0 & -\frac{uv \cos \xi}{2\sqrt{\pi}} \end{pmatrix}. \tag{S13}
\end{aligned}$$

It turns out that $\mathbf{D}^z = 0$, $\mathbf{D}^x = D_x \cos \omega_0 t$, and $\mathbf{D}^y = D_y \sin \omega_0 t$, where

$$\begin{aligned}
D_x &= -2d\sqrt{\frac{2\pi}{3}} \sum_{j=1,2} (\langle \hat{d}_{p,j}^+ \rangle + \langle \hat{d}_{m,j}^+ \rangle), \\
D_y &= 2d\sqrt{\frac{2\pi}{3}} \sum_{j=1,2} (\langle \hat{d}_{p,j}^+ \rangle - \langle \hat{d}_{m,j}^+ \rangle). \tag{S14}
\end{aligned}$$

In Fig. S1, we show $|D_x|$ and $|D_y|$ as the function of Ω and ξ , where the sum $\mathbf{D}_{\text{tot}} \equiv d \sum_j \langle +, + | \hat{\mathbf{d}}_j | +, + \rangle$ of dipole moments for two widely separated molecules is also plotted as a reference.

S2. COUPLED-CHANNEL SCATTERING CALCULATIONS

In this section, we perform the multi-channel scattering calculations to obtain the accurate binding energy and the life-time of the tetramer state. The multi-channel SE reads

$$\sum_{\nu'=1}^7 \left(-\frac{\nabla^2}{M} \delta_{\nu\nu'} + V_{\nu\nu'} \right) \psi_{\nu'}(\mathbf{r}) = E \psi_{\nu}(\mathbf{r}), \tag{S15}$$

where $E = k^2/M + \mathcal{E}_{\nu_0}$ is the incident energy of the ν_0 th channel. We expand $\psi_{\nu}(\mathbf{r}) = \sum_{lm} r^{-1} \phi_{\nu lm} Y_{lm}(\hat{\mathbf{r}})$ in the angular momentum basis, where l is even (odd) for bosons (fermions). The Schrödinger equation for $\phi_{\nu lm}$ follows from Eq. (S15) as

$$\sum_{\nu' l' m'} \left[\left(-\frac{\partial^2}{\partial r^2} + \frac{l(l+1)}{r^2} - \frac{MC_{\text{vdW}}}{r^6} \right) \delta_{\nu\nu'} \delta_{ll'} \delta_{mm'} - \frac{Md^2}{4\pi\epsilon_0 r^3} \sum_{s=-2}^2 (\Xi_s)_{\nu lm, \nu' l' m'} \right] \phi_{\nu' l' m'}(r) = k_{\nu}^2 \phi_{\nu lm}(r), \tag{S16}$$

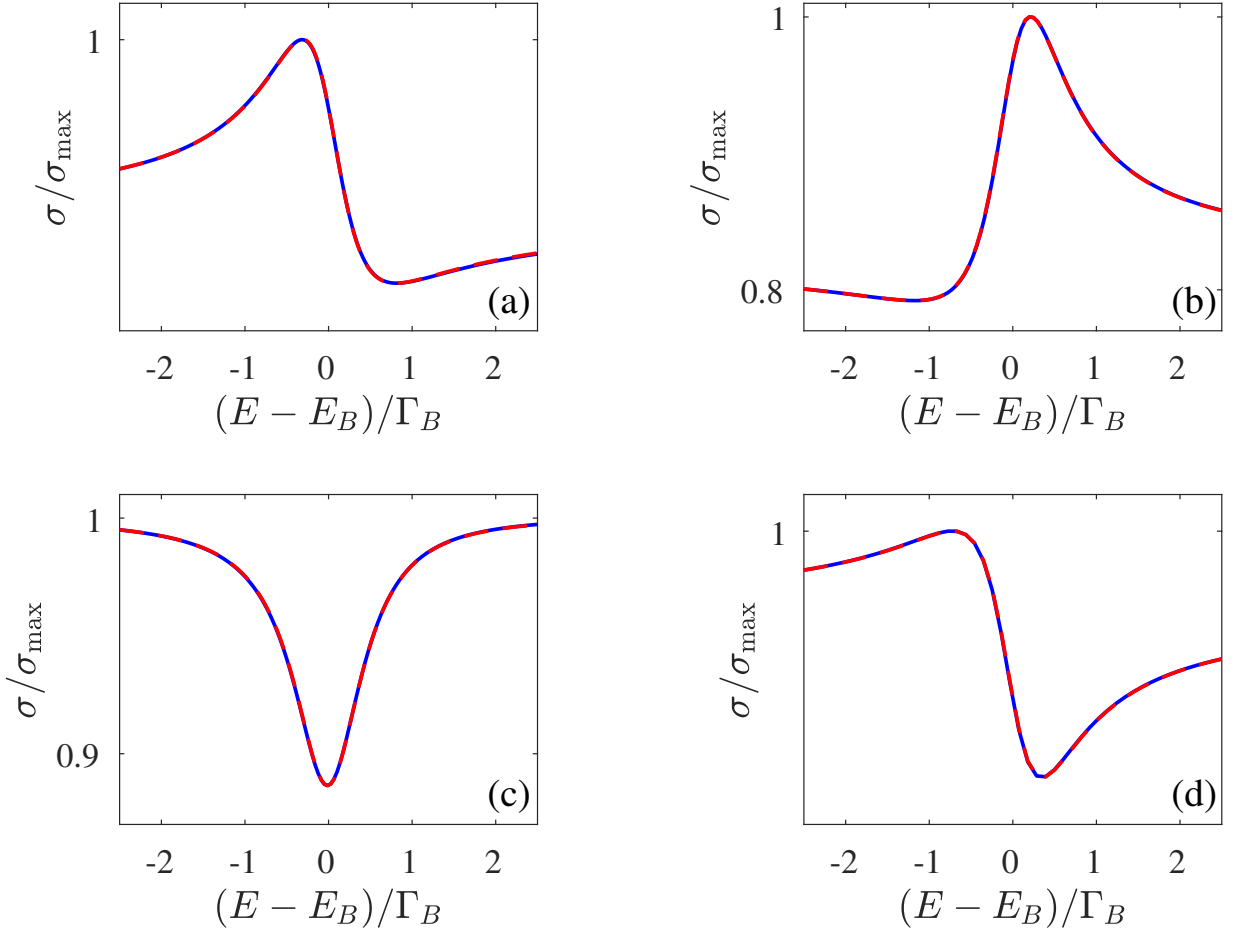


FIG. S2. Comparisons of lineshapes obtained from coupled channel calculations and Eq. (2) in the main text, where $\delta/(2\pi) = -9.5\text{MHz}$: (a) $(\Omega/(2\pi), \xi) = (19.52 \text{ MHz}, 10^\circ)$ and (b) $(\Omega/(2\pi), \xi) = (61.58 \text{ MHz}, 2^\circ)$ display the lineshapes around the resonance with the p_y -tetramer state $|\psi_{B,+}\rangle$; (c) $(\Omega/(2\pi), \xi) = (148.94 \text{ MHz}, 2^\circ)$ and (d) $(\Omega/(2\pi), \xi) = (243.59 \text{ MHz}, 4^\circ)$ display the lineshapes around the resonance with the p_x -tetramer state $|\psi_{B,-}\rangle$.

where $k_\nu = \sqrt{k^2 + M(\mathcal{E}_{\nu_0} - \mathcal{E}_\nu)}$ and

$$(\Xi_s)_{\nu l m, \nu' l' m'} = 4\pi \sqrt{\frac{2(2l'+1)}{3(2l+1)}} C_{l'020}^{l0} C_{l'm'2s}^{lm} (\Sigma_{2,s}^\dagger)_{\nu\nu'} \quad (\text{S17})$$

$C_{l'm'l'm''}^{lm}$ being the short-hand notation for the Clebsch-Gordan coefficients. In the compact form, Eq. (S16) reads

$$\left[\frac{\partial^2}{\partial r^2} + \mathcal{V}(r) \right] \phi(r) = 0, \quad (\text{S18})$$

where the potential

$$\mathcal{V}(r) = \left[k_\nu^2 - \frac{l(l+1)}{r^2} + \frac{MC_{\text{vdW}}}{r^6} \right] \delta_{\nu\nu'} \delta_{ll'} \delta_{mm'} + \frac{Md^2}{4\pi\epsilon_0 r^3} \sum_{s=-2}^2 (\Xi_s)_{\nu l m, \nu' l' m'}. \quad (\text{S19})$$

The coupled channel SE (S18) can be solved using the log-derivative method [S72] with high precision. To describe the formation of the four body complex inside the shielding core, we employ the capture boundary condition [S65, S73] at $r = r_0$. We note that since the wavefunction has a tiny distribution inside the shielding core the result is not affected by the choice of $r_0 < 10^2 a_0$. In the numerical calculation, the result is stable for different choices $r_0 = 32a_0$, $48.5a_0$, and $64a_0$.

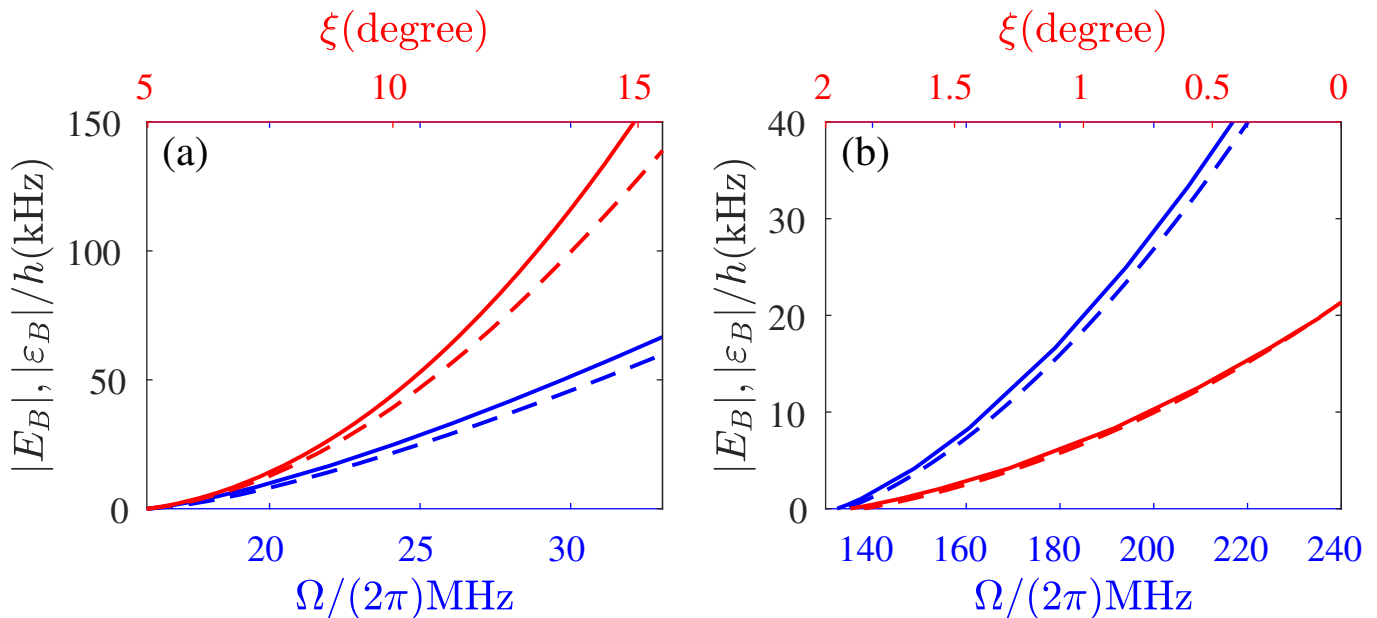


FIG. S3. Comparisons of binding energies obtained from fitting lineshapes to Eq. (2) in the main text (solid curves) and the effective potential (dashed curves), where $\delta/(2\pi) = -9.5\text{MHz}$. (a) The blue and red curves display binding energies of the p_y -tetramer state along the horizontal and vertical cuts in Fig. 1c of the main text; (b) The blue and red curves display binding energies of the p_x -tetramer state along the horizontal and vertical cuts in Fig. 1d of the main text.

By matching the numerical solution with the asymptotic wavefunction, we can obtain the scattering K -matrix, which results in the scattering amplitude

$$f_{\nu l m}^{\nu' l' m'} = i \frac{1}{\sqrt{k_{\nu'}}} \left(\frac{1}{K + i} K \right)_{\nu' l' m', \nu l m} \frac{1}{\sqrt{k_{\nu}}} \quad (\text{S20})$$

from the channel $(\nu l m)$ to the channel $(\nu' l' m')$, and the partial wave scattering cross section $\sigma_{\nu l m}^{\nu' l' m'} = 4\pi \left| f_{\nu l m}^{\nu' l' m'} \right|^2$. We can also obtain the average elastic and inelastic scattering cross sections $\sigma_{\nu}^{\text{el}} = \sum_{l m l' m'} \sigma_{\nu l m}^{\nu' l' m'}$ and $\sigma_{\nu}^{\text{inel}} = \sum_{\nu', l m l' m'} k_{\nu'} \sigma_{\nu l m}^{\nu' l' m'} / k_{\nu}$.

In Fig. S2, we show the scattering cross sections σ_{210}^{210} , which display perfect agreement with the analytical expression (2) in the main text for the Feshbach resonances. We show the binding energy $|E_B|$ and the decay rate Γ_B of the tetramer state extracted from the lineshape in the main text. Here, in Fig. S3 we present the comparison between $|E_B|$ and the binding energy ε_B obtained from the effective potential.

We note that the lifetime of the p_x -tetramer state for LiBb molecules can be extended to 10.4s for the system parameters $\xi = 0.5$, $\delta = 2\pi \times 1\text{MHz}$, and $\Omega = 2\pi \times 98.3\text{MHz}$.

S3. TETRAMER ASSOCIATIONS AND DISSOCIATIONS

The tetramer association can be simulated by evolving the time-dependent SE corresponding to the effective Hamiltonian $H_{\text{eff}}(t)$, where C_3 , C_6 , and \mathcal{F}_{ξ} are time-dependent. The conversion efficiency [S67]

$$\mathcal{E}_A = 2n\lambda_T^3 \int d\mathbf{k} e^{-\beta \frac{k^2}{M}} p_a(\mathbf{k}) \quad (\text{S21})$$

to the tetramer can be evaluated using the density n of molecular gases and the thermal de Broglie wavelength $\lambda_T = (4\pi\hbar^2/MT)^{1/2}$ at temperature T , where the transition probability $p_a(\mathbf{k}) = |\langle \psi_B | U(\tau_a) | \psi_{\mathbf{k}} \rangle|^2$ in the association time τ_a is determined by the unitary evolution operator $U(\tau_a) = \mathcal{T} \exp[-i \int_0^{\tau_a} dt H_{\text{eff}}(t)]$. Here, the initial state $|\psi_{\mathbf{k}}\rangle$ is the scattering eigenstate of $H_{\text{eff}}(0)$, and the final state $|\psi_B\rangle$ is the tetramer state of $H_{\text{eff}}(\tau_a)$.

In the left and right panels of Fig. S4, we show the conversion efficiency \mathcal{E}_A as a function of ramp speeds $v_{\Omega} = \partial_t \Omega$ and $v_{\xi} = \partial_t \xi$, respectively. In the first and second rows, \mathcal{E}_A for the p_y - and p_x -tetramer states are plotted. Adiabaticity is

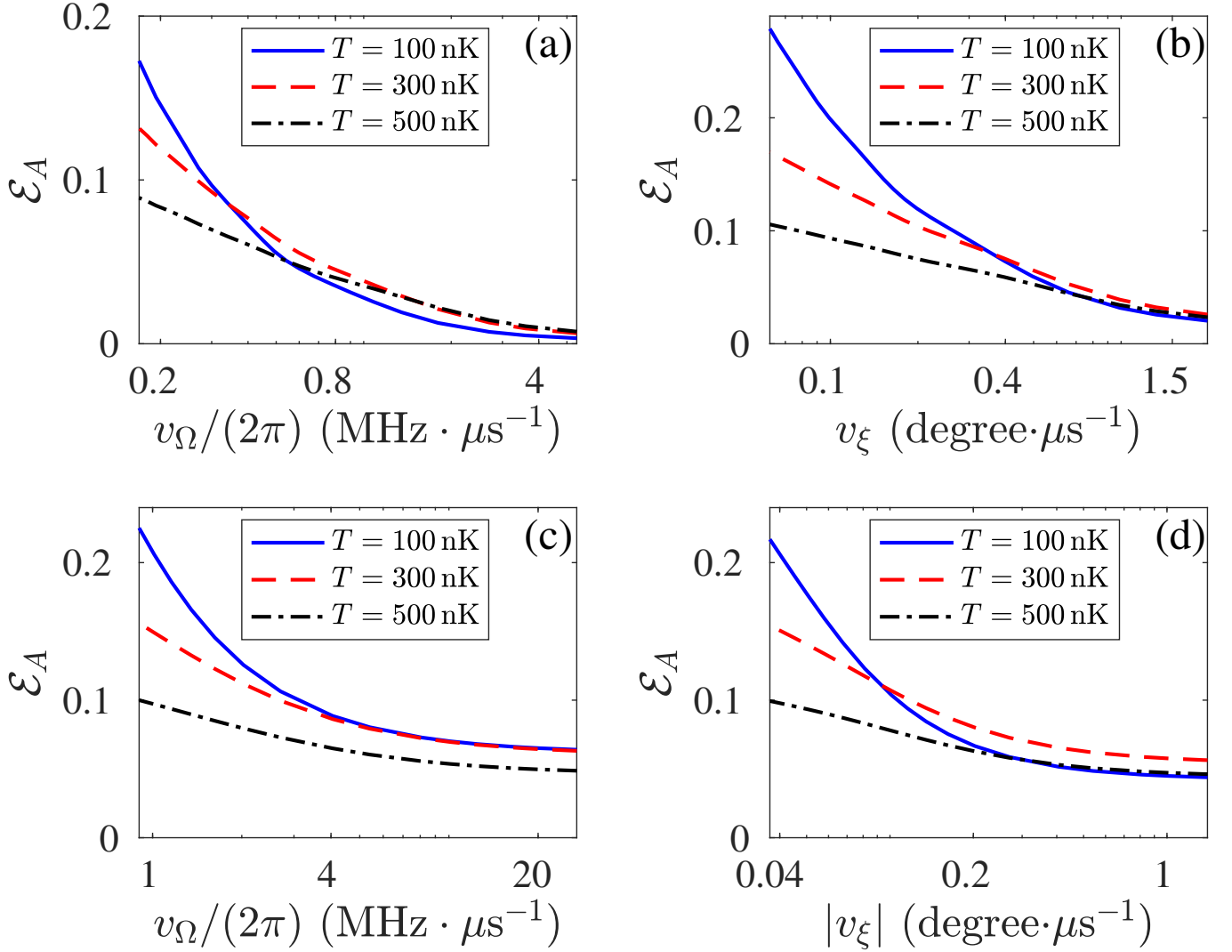


FIG. S4. Association efficiency as a function of ramp speeds $v_\Omega = \partial_t \Omega$ and $v_\xi = \partial_t \xi$, respectively. (a) For $\xi = 10^\circ$, the ramp of $\Omega/(2\pi)$ from 5MHz to 35MHz with speed v_Ω ; (b) For $\Omega/(2\pi) = 28.5\text{MHz}$, the ramp of ξ from 1° to 12° with speed v_ξ ; (c) For $\xi = 2^\circ$, the ramp of $\Omega/(2\pi)$ from 80MHz to 170MHz with speed v_Ω ; (d) For $\Omega/(2\pi) = 150\text{MHz}$, the ramp of ξ from 5° to 0.5° with speed v_ξ .

crucial for high conversion efficiency, and slower ramps lead to higher adiabaticity. Additionally, for slow ramp speeds, the conversion efficiency to tetramer states is higher at lower temperatures T . It should be noted that this result, obtained from two-body scattering calculations, is not valid in the saturation regime of \mathcal{E}_A [S74], where many-body effects must be considered using the non-Markovian Boltzmann equation.

A reverse fast ramp leads to the dissociation of tetramers initially at the temperature T . After the dissociation process, the wavefunction $\psi_d(\mathbf{k}) = \langle \mathbf{k} | U(\tau) | \psi_B^{(x,y)} \rangle$ in the center of mass frame is obtained using the B-spline method,

where \mathbf{k} is the relative momentum. The momentum distribution of the molecule dissociated from the tetramer is

$$\begin{aligned}
n_T(\mathbf{k}) &= \frac{1}{(4\pi MT)^{3/2}} \int d\mathbf{p} e^{-\beta \frac{(\mathbf{k}+\mathbf{p})^2}{4M}} \left| \psi_d\left(\frac{\mathbf{k}-\mathbf{p}}{2}\right) \right|^2 \\
&= \frac{8}{(4\pi MT)^{3/2}} \int d\mathbf{p} e^{-\beta \frac{(\mathbf{k}-\mathbf{p})^2}{M}} |\psi_d(\mathbf{p})|^2 \\
&= \int d\mathbf{r} e^{-i\mathbf{k}\cdot\mathbf{r}} e^{-\frac{M}{4\beta} r^2} \int \frac{d\mathbf{p}}{(2\pi)^3} e^{i\mathbf{p}\cdot\mathbf{r}} |\psi_d(\mathbf{p})|^2 \\
&= \frac{2}{\pi} \sum_{lm} Y_{lm}(\hat{k}) \int r^2 dr e^{-\frac{M}{4\beta} r^2} j_l(kr) \int p^2 dp j_l(pr) \int d\Omega_p Y_{lm}^*(\hat{p}) |\psi_d(\mathbf{p})|^2.
\end{aligned} \tag{S22}$$

The energy distributions reads

$$\begin{aligned}
f_T(E) &= \int d\mathbf{k} \delta(E - \frac{k^2}{2M}) n_T(\mathbf{k}) \\
&= \int d\mathbf{K} d\mathbf{k} \delta(E - \frac{1}{2M} (\frac{\mathbf{K}}{2} + \mathbf{k})^2) \frac{1}{(4\pi MT)^{3/2}} e^{-\beta \frac{K^2}{4M}} |\psi_d(\mathbf{k})|^2 \\
&= 2\pi \int d\mathbf{k} |\psi_d(\mathbf{k})|^2 \int K^2 dK \int d\cos\theta_K \delta(E - \frac{1}{2M} (\frac{K^2}{4} + k^2) - \frac{Kk}{2M} \cos\theta_K) \frac{e^{-\beta \frac{K^2}{4M}}}{(4\pi MT)^{3/2}} \\
&= \int d\mathbf{k} |\psi_d(\mathbf{k})|^2 \frac{M}{k} 4\pi \int K dK \frac{e^{-\beta \frac{K^2}{4M}}}{(4\pi MT)^{3/2}} \theta(E - \frac{1}{2M} (\frac{K}{2} - k)^2) \theta(\frac{1}{2M} (\frac{K}{2} + k)^2 - E) \\
&= \int d\mathbf{k} |\psi_d(\mathbf{k})|^2 \frac{M}{k(\pi MT)^{1/2}} [e^{-\frac{\beta}{M}(k-\sqrt{2ME})^2} - e^{-\frac{\beta}{M}(k+\sqrt{2ME})^2}].
\end{aligned} \tag{S23}$$

In Fig. S5, for the p_y - and p_x -tetramers, we show the energy distributions $f_T(E)$ in final states of ramp dissociations with different ramp speeds, where the thermal distribution at $T = 100\text{nK}$ is plotted for reference. In insets, the dissociation energy E_{diss} is displayed. The energy distributions via ramps of Ω and ξ exhibit a similar structure.

S4. EFFECTIVE HAMILTONIAN FOR MODULATIONAL DISSOCIATIONS

In this section, we derive the effective Hamiltonian to describe the dissociation under small modulations of the elliptic angle. For two molecules in the highest adiabatic channel, the system is described by $H_{\text{eff}}(\xi) = -\nabla^2/M + V_{\text{eff}}(\mathbf{r})$. When the elliptic angle ξ is modulated, C_6 and $\mathcal{F}_\xi(\varphi)$ in $V_{\text{eff}}(\mathbf{r})$, which depend on ξ , are both time-dependent. For a small modulation $\xi = \xi_0 + \delta\xi \sin \omega_m t$ around the background value ξ_0 , the Taylor expansion leads to

$$H_{\text{eff}}(\xi) \sim H_{\text{eff}}(\xi_0) + \delta\xi \partial_{\xi_0} V_{\text{eff}}(\mathbf{r}) \sin \omega_m t, \tag{S24}$$

where in the explicit form

$$\begin{aligned}
\partial_{\xi_0} V_{\text{eff}}(\mathbf{r}) &= 6 \frac{C_3}{r^3} \cos 2\xi_0 \sin^2 \theta \cos 2\varphi \\
&\quad + \frac{\partial_{\xi_0} C_6}{r^6} \sin^2 \theta \{1 - \mathcal{F}_{\xi_0}^2(\varphi) + [1 - \mathcal{F}_{\xi_0}(\varphi)]^2 \cos^2 \theta\} \\
&\quad - 2 \frac{C_6}{r^6} \sin^2 \theta (\sin 4\xi_0 \sin^2 \theta \cos^2 2\varphi + 2 \cos 2\xi_0 \cos^2 \theta \cos 2\varphi).
\end{aligned} \tag{S25}$$

We use the relation

$$\begin{aligned}
\sin^2 \theta \cos 2\varphi &= 2\sqrt{\frac{2\pi}{15}} (Y_{22} + Y_{2-2}), \\
\sin^2 \theta (1 + \cos^2 \theta) &= \frac{4}{5} - \frac{8}{7}\sqrt{\frac{\pi}{5}} Y_{20} - \frac{16\sqrt{\pi}}{105} Y_{40}, \\
\sin^2 \theta \cos^2 \theta \cos 2\varphi &= \frac{2}{7}\sqrt{\frac{2\pi}{15}} (Y_{22} + Y_{2-2}) + \frac{4}{21}\sqrt{\frac{2\pi}{5}} (Y_{42} + Y_{4-2}), \\
\sin^4 \theta \cos^2 2\varphi &= \frac{4}{15} - \frac{16}{21}\sqrt{\frac{\pi}{5}} Y_{20} + \frac{8\sqrt{\pi}}{105} Y_{40} + \frac{4}{3}\sqrt{\frac{2\pi}{35}} (Y_{44} + Y_{4-4})
\end{aligned} \tag{S26}$$

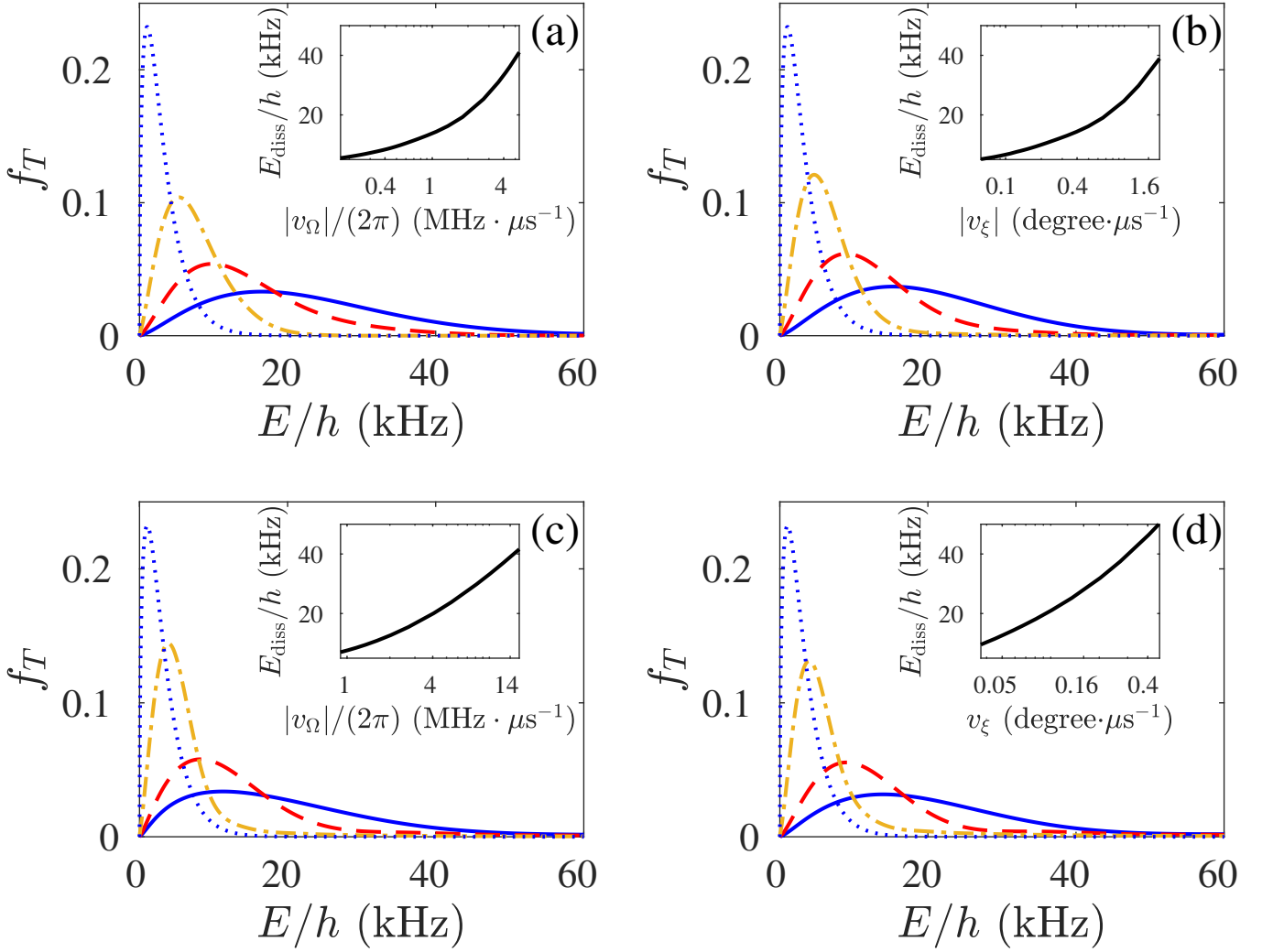


FIG. S5. Ramp dissociations for the the p_y - and p_x -tetramers (in the first and second rows) with different ramp speeds, alongside the thermal distribution at $T = 100\text{nK}$ for reference (dashed blue curves). (a) For $\xi = 10^\circ$, the ramp of $\Omega/(2\pi)$ from 35MHz to 5MHz with speed $v_\Omega/(2\pi) = 0.45\text{MHz}/\mu\text{s}$ (the yellow dash-dotted curve), $1.36\text{MHz}/\mu\text{s}$ (the red dashed curve), and $2.73\text{MHz}/\mu\text{s}$ (the blue solid curve); (b) For $\Omega/(2\pi) = 28.5\text{MHz}$, the ramp of ξ from 12° to 1° with speed $v_\xi = 0.17^\circ/\mu\text{s}$ (the yellow dash-dotted curve), $0.5^\circ/\mu\text{s}$ (the red dashed curve), and $1^\circ/\mu\text{s}$ (the blue solid curve); (c) For $\xi = 2^\circ$, the ramp of $\Omega/(2\pi)$ from 170MHz to 80MHz with speed $v_\Omega/(2\pi) = 1.36\text{MHz}/\mu\text{s}$ (the yellow dash-dotted curve), $4.09\text{MHz}/\mu\text{s}$ (the red dashed curve), and $8.18\text{MHz}/\mu\text{s}$ (the blue solid curve); (d) For $\Omega/(2\pi) = 150\text{MHz}$, the ramp of ξ from 0.5° to 5° with speed $v_\xi = 0.07^\circ/\mu\text{s}$ (the yellow dash-dotted curve), $0.2^\circ/\mu\text{s}$ (the red dashed curve), and $0.41^\circ/\mu\text{s}$ (the blue solid curve). The insets show E_{diss} as functions of ramp speeds. The thermal distribution at $T = 100\text{nK}$ is shown by the dashed blue curve for reference.

to re-express

$$\begin{aligned}
\partial_{\xi_0} V_{\text{eff}}(\mathbf{r}) = & 12\sqrt{\frac{2\pi}{15}} \frac{C_3}{r^3} \cos 2\xi_0 (Y_{22} + Y_{2-2}) + \frac{1}{r^6} \partial_{\xi_0} C_6 \left(\frac{4}{5} - \frac{8}{7} \sqrt{\frac{\pi}{5}} Y_{20} - \frac{16\sqrt{\pi}}{105} Y_{40} \right) \\
& - \frac{2}{r^6} (2C_6 \cos 2\xi_0 + \partial_{\xi_0} C_6 \sin 2\xi_0) \left[\frac{2}{7} \sqrt{\frac{2\pi}{15}} (Y_{22} + Y_{2-2}) + \frac{4}{21} \sqrt{\frac{2\pi}{5}} (Y_{42} + Y_{4-2}) \right] \\
& - \frac{1}{r^6} (2C_6 \sin 4\xi_0 + \partial_{\xi_0} C_6 \sin^2 2\xi_0) \left[\frac{4}{15} - \frac{16}{21} \sqrt{\frac{\pi}{5}} Y_{20} + \frac{8\sqrt{\pi}}{105} Y_{40} + \frac{4}{3} \sqrt{\frac{2\pi}{35}} (Y_{44} + Y_{4-4}) \right] \quad (\text{S27})
\end{aligned}$$

in terms of spherical harmonics.

In the eigen-basis $\{|\psi_B\rangle, |\psi_{\mathbf{k}}\rangle\}$ of $H_{\text{eff}}(\xi_0)$, the Hamiltonian becomes

$$H_{\text{eff}}(\xi) = \varepsilon_B |\psi_B\rangle \langle \psi_B| + \int d\mathbf{k} \varepsilon_{\mathbf{k}} |\psi_{\mathbf{k}}\rangle \langle \psi_{\mathbf{k}}| + \delta\xi \sin \omega_m t \int d\mathbf{k} \langle \psi_{\mathbf{k}} | \partial_{\xi_0} V_{\text{eff}}(\mathbf{r}) | \psi_B \rangle |\psi_{\mathbf{k}}\rangle \langle \psi_B| + \text{H.c.} \\ + \delta\xi \sin \omega_m t [\langle \psi_B | \partial_{\xi_0} V_{\text{eff}}(\mathbf{r}) | \psi_B \rangle |\psi_B\rangle \langle \psi_B| + \int d\mathbf{k} d\mathbf{k}' \langle \psi_{\mathbf{k}} | \partial_{\xi_0} V_{\text{eff}}(\mathbf{r}) | \psi_{\mathbf{k}'} \rangle |\psi_{\mathbf{k}}\rangle \langle \psi_{\mathbf{k}'}|], \quad (\text{S28})$$

where $\varepsilon_{\mathbf{k}} = k^2/M$. For the large dissociation frequency ω_m , the rotating-wave-approximation (RWA) results in

$$H_{\text{eff}}(\xi) \sim \varepsilon_B |\psi_B\rangle \langle \psi_B| + \int d\mathbf{k} \varepsilon_{\mathbf{k}} |\psi_{\mathbf{k}}\rangle \langle \psi_{\mathbf{k}}| + e^{-i\omega_m t} \int \frac{d\mathbf{k}}{(2\pi)^{3/2}} g_{\mathbf{k}} |\psi_{\mathbf{k}}\rangle \langle \psi_B| + \text{H.c.}, \quad (\text{S29})$$

where

$$g_{\mathbf{k}} = i \frac{1}{2} \delta\xi (2\pi)^{3/2} \langle \psi_{\mathbf{k}} | \partial_{\xi_0} V_{\text{eff}} | \psi_B \rangle. \quad (\text{S30})$$

In the interaction picture, we obtain the dissociation Hamiltonian $H_{\text{eff}}(\xi) \sim H_{\text{diss}}$:

$$H_{\text{diss}} = (\varepsilon_B + \omega_m) |\psi_B\rangle \langle \psi_B| + \int d\mathbf{k} \varepsilon_{\mathbf{k}} |\psi_{\mathbf{k}}\rangle \langle \psi_{\mathbf{k}}| + \int \frac{d\mathbf{k}}{(2\pi)^{3/2}} (g_{\mathbf{k}} |\psi_{\mathbf{k}}\rangle \langle \psi_B| + \text{H.c.}). \quad (\text{S31})$$

Using the numerical solutions

$$\psi_B(r) = \sum_{lm} \frac{\phi_{lm}(r)}{r} Y_{lm}(r), \\ \psi_{\mathbf{k}}(r) = \sum_{lm} \frac{\varphi_{\mathbf{k},lm}(r)}{r} Y_{lm}(r). \quad (\text{S32})$$

of the bound-state and the scattering-state wavefunctions obtained from the B-spline algorithm, we obtain the Frank-Condon factor

$$g_{\mathbf{k}} = i \frac{1}{2} \delta\xi (2\pi)^{3/2} \sum_{lm'l'm'} \sqrt{\frac{2l'+1}{2l+1}} \times \\ \{ 2\sqrt{6} C_3 \cos 2\xi_0 C_{20l'0}^{l0} (C_{22l'm'}^{lm} \delta_{mm'+2} + C_{2-2l'm'}^{lm} \delta_{mm'-2}) \int_0^\infty dr \frac{1}{r^3} \varphi_{\mathbf{k},lm}^*(r) \phi_{l'm'}(r) \\ + \partial_{\xi_0} C_6 (\frac{4}{5} \delta_{ll'} - \frac{4}{7} C_{20l'0}^{l0} C_{20l'm}^{lm} - \frac{8}{35} C_{40l'0}^{l0} C_{40l'm}^{lm}) \delta_{mm'} \int_0^\infty dr \frac{1}{r^6} \varphi_{\mathbf{k},lm}^*(r) \phi_{l'm'}(r) \\ - \frac{2}{7} (2C_6 \cos 2\xi_0 + \partial_{\xi_0} C_6 \sin 2\xi_0) [\sqrt{\frac{2}{3}} C_{20l'0}^{l0} (C_{22l'm'}^{lm} \delta_{mm'+2} + C_{2-2l'm'}^{lm} \delta_{mm'-2}) \\ + 2\sqrt{\frac{2}{5}} C_{40l'0}^{l0} (C_{42l'm'}^{lm} \delta_{mm'+2} + C_{4-2l'm'}^{lm} \delta_{mm'-2})] \int_0^\infty dr \frac{1}{r^6} \varphi_{\mathbf{k},lm}^*(r) \phi_{l'm'}(r) \\ - (2C_6 \sin 4\xi_0 + \partial_{\xi_0} C_6 \sin^2 2\xi_0) [\frac{4}{15} \delta_{ll'} \delta_{mm'} - \frac{8}{21} C_{20l'0}^{l0} C_{20l'm}^{lm} \delta_{mm'} + \frac{4}{35} C_{40l'0}^{l0} C_{40l'm}^{lm} \delta_{mm'} \\ + \sqrt{\frac{8}{35}} C_{40l'0}^{l0} (C_{44l'm'}^{lm} \delta_{mm'+4} + C_{4-4l'm'}^{lm} \delta_{mm'-4})] \int_0^\infty dr \frac{1}{r^6} \varphi_{\mathbf{k},lm}^*(r) \phi_{l'm'}(r) \}. \quad (\text{S33})$$

S5. DISSOCIATION SPECTRUM AND MOMENTUM DISTRIBUTION

In this section, we derive the analytic formula for the dissociation spectrum P_{diss} and the momentum distribution $p_{\mathbf{m}}(\mathbf{k})$ of two dissociated molecules using the dissociation Hamiltonian H_{diss} for the small $\delta\xi$. We rewrite the dissociation Hamiltonian as

$$H_{\text{diss}} = (\varepsilon_B + \omega_m) B^\dagger B + \int d\mathbf{k} \varepsilon_{\mathbf{k}} a_{\mathbf{k}}^\dagger a_{\mathbf{k}} + \int \frac{d\mathbf{k}}{(2\pi)^{3/2}} (g_{\mathbf{k}} a_{\mathbf{k}}^\dagger B + \text{H.c.}), \quad (\text{S34})$$

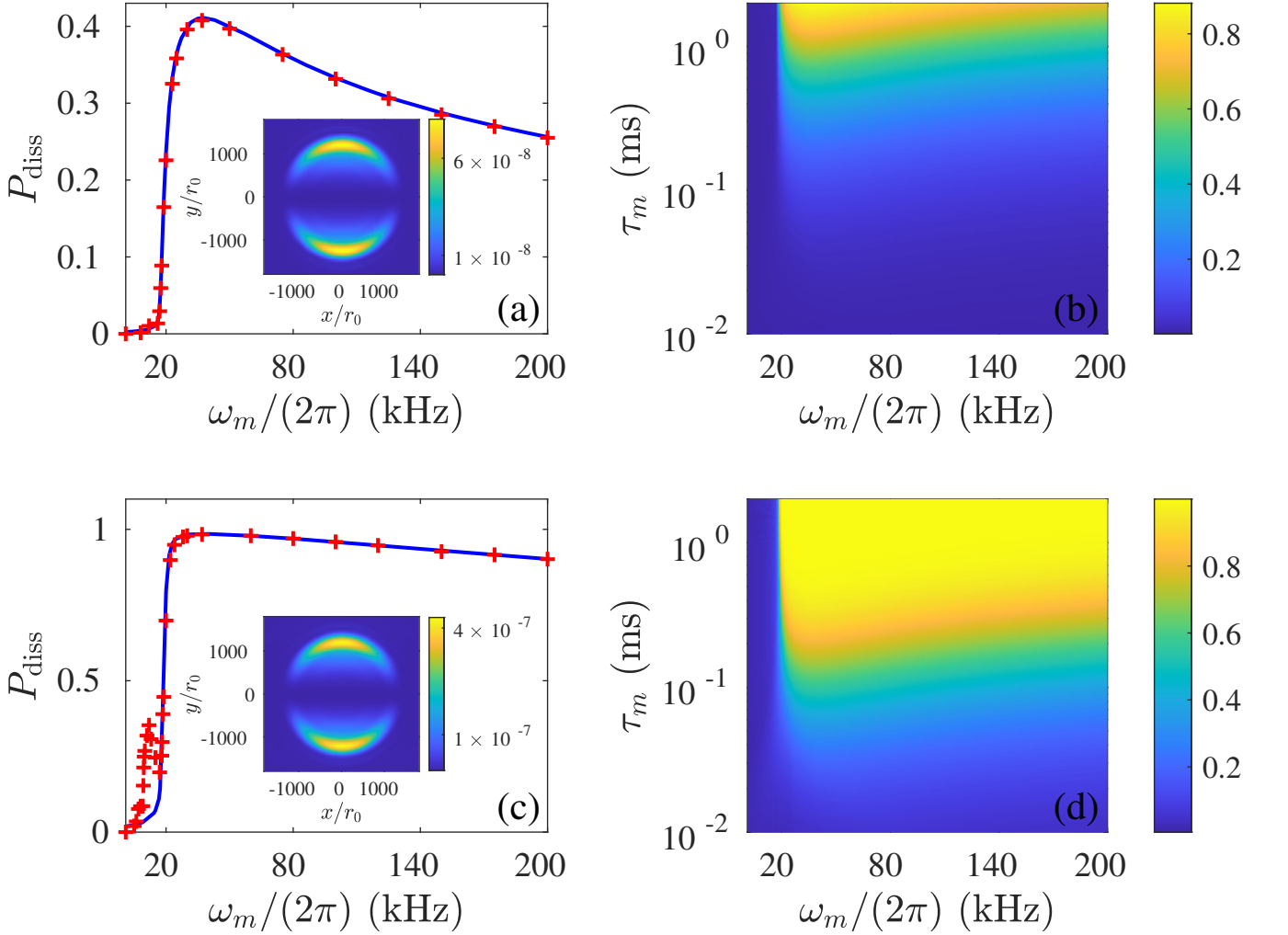


FIG. S6. Modulation dissociation spectra for the p_y -tetramer state $|\psi_B^{(y)}\rangle$, where $(\Omega, \delta)/(2\pi) = (28.5, -9.5)\text{MHz}$ and $\xi_0 = 8^\circ$. The first and second rows displays P_{diss} for $\delta\xi = 0.5^\circ$ and $\delta\xi = 1.4^\circ$, respectively. The first panel displays P_{diss} at $\tau_m = 0.5\text{ms}$, where the blue curves and red crosses represent the RWA and exact results, respectively. The insets show the coordinate distribution integrated along the z -direction at 3ms in TOF after the dissociation with modulation frequency $\omega_m/(2\pi) = 37\text{kHz}$. The second column displays P_{diss} under RWA in the ω_m - τ_m plane.

which explicitly describes the spontaneous emission of the tetramer state to the continuum. The dissociation spectrum $P_{\text{diss}} = 1 - |G_B(t)|^2$ and the momentum distribution $p_m(\mathbf{k}) = |\int d\mathbf{p} \langle \mathbf{k} | \psi_{\mathbf{p}} \rangle G_{\mathbf{p}}(t)|^2$ are determined by the time-ordered Green functions $G_B(t) = -i \langle 0 | \mathcal{T} B(t) B^\dagger(0) | 0 \rangle$ and $G_{\mathbf{p}}(t) = -i \langle 0 | \mathcal{T} a_{\mathbf{p}}(t) B^\dagger(0) | 0 \rangle$.

The Dyson expansion leads to the Green functions

$$\begin{aligned} G_B(t) &= \int \frac{d\omega}{2\pi} \frac{e^{-i\omega t}}{\omega - \varepsilon_0 - \Sigma(\omega)}, \\ G_{\mathbf{p}}(t) &= \frac{g_{\mathbf{p}}}{(2\pi)^{3/2}} \int \frac{d\omega}{2\pi} \frac{e^{-i\omega t}}{\omega - \varepsilon_{\mathbf{p}} + i0^+} \frac{1}{\omega - \varepsilon_0 - \Sigma(\omega)}, \end{aligned} \quad (\text{S35})$$

where $\varepsilon_0 = \varepsilon_B + \omega_m$ and the self-energy

$$\Sigma(\omega) = \int \frac{d\mathbf{k}}{(2\pi)^3} \frac{|g_{\mathbf{k}}|^2}{\omega - \varepsilon_{\mathbf{k}} + i0^+}. \quad (\text{S36})$$

Under the Markovian approximation, the self-energy reads

$$\Sigma(\omega) = \int \frac{d\mathbf{k}}{(2\pi)^3} \text{P} \frac{|g_{\mathbf{k}}|^2}{\omega - \varepsilon_{\mathbf{k}}} - i\pi \int \frac{d\mathbf{k}}{(2\pi)^3} |g_{\mathbf{k}}|^2 \delta(\omega - \varepsilon_{\mathbf{k}}) \sim -i\frac{1}{2}\gamma_{\text{diss}}, \quad (\text{S37})$$

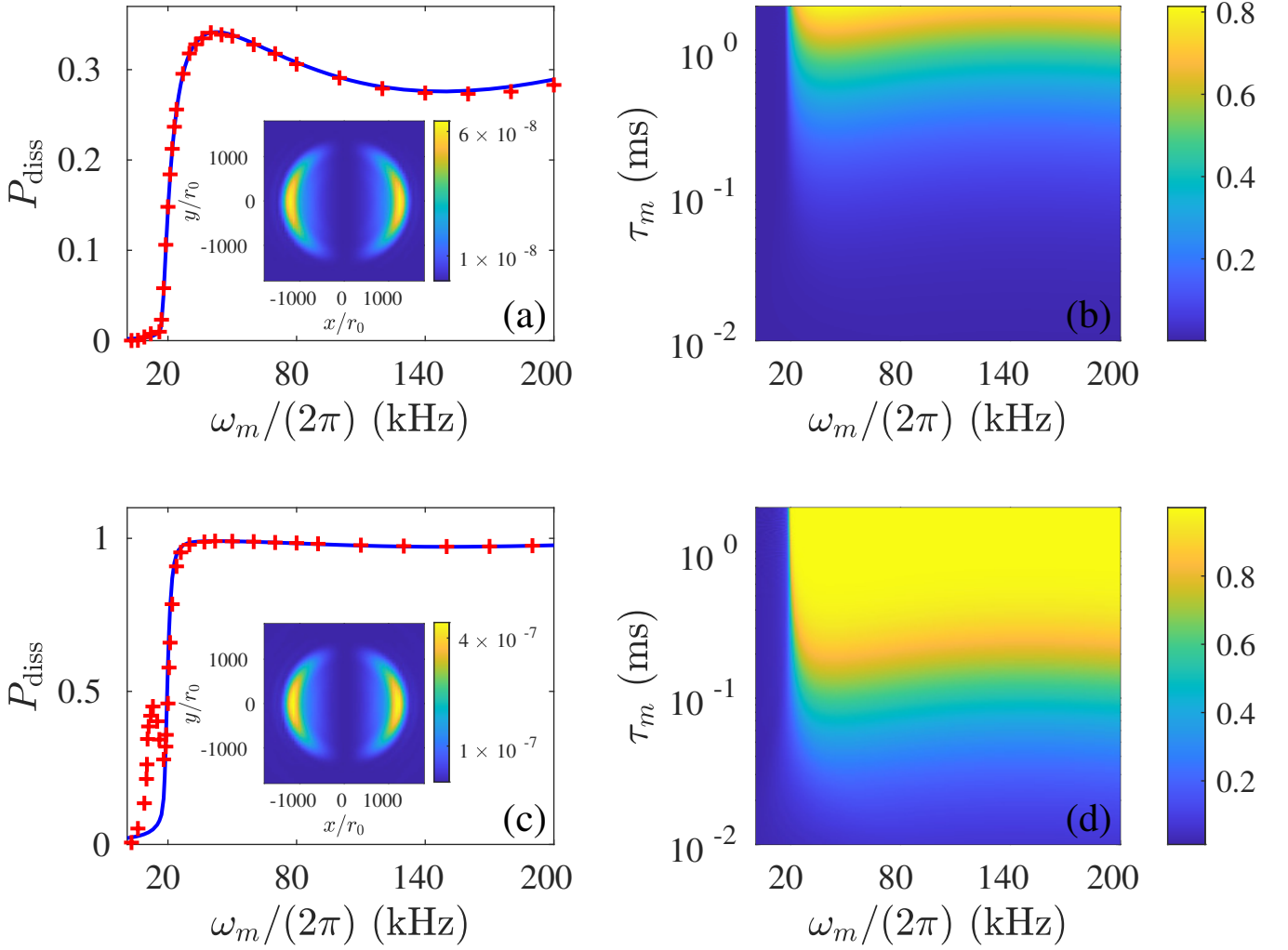


FIG. S7. Modulation dissociation spectra for the p_x -tetramer state $|\psi_B^{(x)}\rangle$, where $(\Omega, \delta)/(2\pi) = (167.2, -9.5)\text{MHz}$ and $\xi_0 = 1.5^\circ$. The first and second rows displays P_{diss} for $\delta\xi = 0.3^\circ$ and $\delta\xi = 1^\circ$, respectively. The first panel displays P_{diss} at $\tau_m = 0.5\text{ms}$, where the blue curves and red crosses represent the RWA and exact results, respectively. The insets show the coordinate distribution integrated along the z -direction at 3ms in TOF after the dissociation with modulation frequency $\omega_m/(2\pi) = 37\text{kHz}$. The second column displays P_{diss} under RWA in the ω_m - τ_m plane.

where we omit the real part of $\Sigma(\omega)$ that renormalizes ε_0 , and define the dissociation rate $\gamma_{\text{diss}} = \int \frac{d\mathbf{k}}{(2\pi)^2} |g_{\mathbf{k}}|^2 \delta(\varepsilon_0 - \varepsilon_{\mathbf{k}})$. It follows from the residue theorem that

$$\begin{aligned} G_B(t) &= -ie^{-\frac{1}{2}\gamma_{\text{diss}}t} e^{-i\varepsilon_0 t}, \\ G_{\mathbf{p}}(t) &= -i \frac{g_{\mathbf{p}}}{(2\pi)^{3/2}} \frac{e^{-i\varepsilon_{\mathbf{p}}t} - e^{-i(\varepsilon_0 - i\frac{1}{2}\gamma_{\text{diss}})t}}{\varepsilon_{\mathbf{p}} - \varepsilon_0 + i\frac{1}{2}\gamma_{\text{diss}}}, \end{aligned} \quad (\text{S38})$$

and

$$\begin{aligned} P_{\text{diss}} &= 1 - e^{-\gamma_{\text{diss}}t}, \\ p_{\mathbf{m}}(\mathbf{k}) &= \left| \int d\mathbf{p} \langle \mathbf{k} | \psi_{\mathbf{p}} \rangle \frac{g_{\mathbf{p}}}{(2\pi)^{3/2}} \frac{e^{-i\varepsilon_{\mathbf{p}}t} - e^{-i(\varepsilon_0 - i\frac{1}{2}\gamma_{\text{diss}})t}}{\varepsilon_{\mathbf{p}} - \varepsilon_0 + i\frac{1}{2}\gamma_{\text{diss}}} \right|^2. \end{aligned} \quad (\text{S39})$$

In the limit $\gamma_{\text{diss}}t_F \ll 1$, $P_{\text{diss}} \sim \gamma_{\text{diss}}t$ agree with that from the Fermi Golden rule, and

$$p_{\mathbf{m}}(\mathbf{k}) \sim \frac{1}{4} \delta\xi^2 |\langle \mathbf{k} | \partial_{\xi_0} V_{\text{eff}} | \psi_B \rangle|^2 t^2. \quad (\text{S40})$$

In Figs. S6 and S7, we compare the exact dissociation spectrum and that obtained using the effective Hamiltonian H_{diss} under RWA for the p_y and p_x -tetramer states, respectively. For small $\delta\xi$, the exact dissociation spectra via solving the time-dependent SE agrees with the RWA result quantitatively in the entire frequency domain. For large $\delta\xi$, the quantitative agreement between the exact result and the RWA result is also shown above the dissociation threshold, however, a below-threshold peak predicted by the exact result is displayed in P_{diss} .

The below-threshold peak corresponds to the multiple-photon process, which can be qualitatively described by the following effective model

$$H_{\text{eff}} = (\varepsilon_B + \delta\omega_B \sin \omega_m t) |\psi_B\rangle \langle \psi_B| + \int d\mathbf{k} \varepsilon_{\mathbf{k}} |\psi_{\mathbf{k}}\rangle \langle \psi_{\mathbf{k}}| - 2i \sin(\omega_m t) \int \frac{d\mathbf{k}}{(2\pi)^{3/2}} g_{\mathbf{k}} |\psi_{\mathbf{k}}\rangle \langle \psi_B| + \text{H.c.}, \quad (\text{S41})$$

where for small modulational frequency ω_m , the large modulation $\delta\xi$ induces the frequency fluctuation $\delta\omega_B = \delta\xi \langle \psi_B | \partial_{\xi_0} V_{\text{eff}}(\mathbf{r}) | \psi_B \rangle$ comparable to ω_m . Thus, the energy level fluctuation of the tetramer state is not negligible.

In the interacting picture, the Hamiltonian reads

$$\bar{H}_{\text{eff}} = \int d\mathbf{k} \varepsilon_{\mathbf{k}} |\psi_{\mathbf{k}}\rangle \langle \psi_{\mathbf{k}}| + e^{-i\varepsilon_B t} \sum_{n,s=\pm 1} s i^n J_n \left(\frac{\delta\omega_B}{\omega_m} \right) e^{-i(n+s)\omega_m t} \int \frac{d\mathbf{k}}{(2\pi)^{3/2}} g_{\mathbf{k}} |\psi_{\mathbf{k}}\rangle \langle \psi_B| + \text{H.c.} \quad (\text{S42})$$

When ω_m is increasing from 0 to the threshold value $|\varepsilon_B|$, the dominating process is the transition from $|\psi_B\rangle$ to $|\psi_{\mathbf{k}}\rangle$ by absorbing $n_0 + 1$ modulation excitations. Under the single frequency approximation, the Hamiltonian becomes

$$\bar{H}_{\text{eff}} \sim \int d\mathbf{k} \varepsilon_{\mathbf{k}} |\psi_{\mathbf{k}}\rangle \langle \psi_{\mathbf{k}}| + e^{-i[\varepsilon_B + (n_0+1)\omega_m]t} i^{n_0} J_{n_0} \left(\frac{\delta\omega_B}{\omega_m} \right) \int \frac{d\mathbf{k}}{(2\pi)^{3/2}} g_{\mathbf{k}} |\psi_{\mathbf{k}}\rangle \langle \psi_B| + \text{H.c.} \quad (\text{S43})$$

By eliminating the time-dependent phase, we obtain

$$\bar{H}_{\text{eff}} \sim [\varepsilon_B + (n_0 + 1)\omega_m] |\psi_B\rangle \langle \psi_B| + \int d\mathbf{k} \varepsilon_{\mathbf{k}} |\psi_{\mathbf{k}}\rangle \langle \psi_{\mathbf{k}}| + i^{n_0} J_{n_0} \left(\frac{\delta\omega_B}{\omega_m} \right) \int \frac{d\mathbf{k}}{(2\pi)^{3/2}} g_{\mathbf{k}} |\psi_{\mathbf{k}}\rangle \langle \psi_B| + \text{H.c.}, \quad (\text{S44})$$

which has the same form as H_{diss} , where the single excitation frequency ω_m is replaced by the multi-excitation frequency $(n_0 + 1)\omega_m$ and $g_{\mathbf{k}} \rightarrow i^{n_0} J_{n_0} \left(\frac{\delta\omega_B}{\omega_m} \right) g_{\mathbf{k}}$. The dissociation studied in Fig. 4b of the main text is a two-photon process, where $n_0 = 1$.